



## Assessing the cloud radiative bias at Macquarie Island in the ACCESS-AM2 model

Zhangcheng Pei<sup>1,2,3</sup>, Sonya L. Fiddes<sup>1,2</sup>, W. John R. French<sup>4,1</sup>, Simon P. Alexander<sup>4,1</sup>, Marc D. Mallet<sup>1</sup>, Peter Kuma<sup>5</sup>, and Adrian McDonald<sup>6</sup>

<sup>1</sup>Australian Antarctic Program Partnership, Institute for Marine and Antarctic Studies,  
University of Tasmania, Hobart, Australia

<sup>2</sup>Australian Research Council Centre of Excellence for Climate Extremes,  
University of Tasmania, Hobart, Australia

<sup>3</sup>College of Oceanic and Atmospheric Sciences, Ocean University of China, Qingdao, China

<sup>4</sup>Australian Antarctic Division, Kingston TAS, Australia

<sup>5</sup>Department of Meteorology, Stockholm University, Stockholm, Sweden

<sup>6</sup>School of Physical and Chemical Sciences, University of Canterbury, Christchurch, Aotearoa/New Zealand

**Correspondence:** Zhangcheng Pei (zhangcheng.pei@utas.edu.au)

Received: 27 February 2023 – Discussion started: 10 March 2023

Revised: 26 September 2023 – Accepted: 28 September 2023 – Published: 29 November 2023

**Abstract.** As a long-standing problem in climate models, large positive shortwave radiation biases exist at the surface over the Southern Ocean, impacting the accurate simulation of sea surface temperature, atmospheric circulation, and precipitation. Underestimations of low-level cloud fraction and liquid water content are suggested to predominantly contribute to these radiation biases. Most model evaluations for radiation focus on summer and rely on satellite products, which have their own limitations. In this work, we use surface-based observations at Macquarie Island to provide the first long-term, seasonal evaluation of both downwelling surface shortwave and longwave radiation in the Australian Community Climate and Earth System Simulator Atmosphere-only Model version 2 (ACCESS-AM2) over the Southern Ocean. The capacity of the Clouds and the Earth's Radiant Energy System (CERES) product to simulate radiation is also investigated. We utilize the novel lidar simulator, the Automatic Lidar and Ceilometer Framework (ALCF), and all-sky cloud camera observations of cloud fraction to investigate how radiation biases are influenced by cloud properties.

Overall, we find an overestimation of  $+9.5 \pm 33.5 \text{ W m}^{-2}$  for downwelling surface shortwave radiation fluxes and an underestimation of  $-2.3 \pm 13.5 \text{ W m}^{-2}$  for downwelling surface longwave radiation in ACCESS-AM2 in all-sky conditions, with more pronounced shortwave biases of  $+25.0 \pm 48.0 \text{ W m}^{-2}$  occurring in summer. CERES presents an overestimation of  $+8.0 \pm 18.0 \text{ W m}^{-2}$  for the shortwave and an underestimation of  $-12.1 \pm 12.2 \text{ W m}^{-2}$  for the longwave in all-sky conditions. For the cloud radiative effect (CRE) biases, there is an overestimation of  $+4.8 \pm 28.0 \text{ W m}^{-2}$  in ACCESS-AM2 and an underestimation of  $-7.9 \pm 20.9 \text{ W m}^{-2}$  in CERES. An overestimation of downwelling surface shortwave radiation is associated with an underestimated cloud fraction and low-level cloud occurrence. We suggest that modeled cloud phase is also having an impact on the radiation biases. Our results show that the ACCESS-AM2 model and CERES product require further development to reduce these radiation biases not just in shortwave and in all-sky conditions, but also in longwave and in clear-sky conditions.

## 1 Introduction

The Southern Ocean (SO) makes up a significant component of the Earth's climate system. As one of the cloudiest regions on Earth, the SO strongly influences the global energy balance and climate (Trenberth et al., 2009; Gettelman et al., 2020). A considerable deficit of reflected shortwave radiation at the top of the atmosphere (TOA) and an excess of absorbed shortwave radiation at the surface over the SO has been identified in both climate models and reanalysis (Trenberth and Fasullo, 2010; Bodas-Salcedo et al., 2014; Kay et al., 2016; Zhang et al., 2016; Fiddes et al., 2022; Cesana et al., 2022; Mallet et al., 2023). Cloud biases tend to limit the capacity of coupled models to accurately derive sea surface temperatures (SSTs) (Hyder et al., 2018), atmospheric circulation (Ceppi et al., 2012), and precipitation (Hwang and Frierson, 2013), as well as to correctly predict future climate changes (Trenberth and Fasullo, 2010; McCoy et al., 2015). As a key driver of global climate, it is important that we unravel what causes these radiative biases over the SO. Previous studies have suggested that the poor representation of clouds in climate models is the main contributor to the radiative biases (Bodas-Salcedo et al., 2012; Franklin et al., 2013; Mason et al., 2015), as clouds primarily control the TOA and surface energy budgets in the climate system (Bennartz et al., 2013; Luo et al., 2016).

Novel techniques including simulators for both satellite retrievals and in situ observations, which are vital for model evaluation, have been developed in recent years. The Cloud Feedback Model Intercomparison Project (CFMIP) Observation Simulator Package (COSP) was created to allow quantitative examination of cloud properties, humidity, and precipitation processes in various numerical models (Bodas-Salcedo et al., 2011). Kuma et al. (2021b) more recently developed the Automatic Lidar and Ceilometer Framework (ALCF) to make automatic lidar and ceilometer (ALC) data comparable with climate models, including both global climate models (GCMs) and numerical weather prediction (NWP) models. Large networks of lidars and ceilometers have been installed globally – for instance, Cloudnet (Illingworth et al., 2007), EPROFILE (Illingworth et al., 2019), and ARM (Campbell et al., 2002). However, surface-based ceilometer observations of cloud frequency of occurrence and cloud boundaries over the SO remain sparse (Kuma et al., 2020). The ALCF can utilize the enormous database of surface-based ceilometer observations to evaluate the cloud occurrence and cloud characteristics in models and reanalysis. This is accomplished by extracting two-dimensional profiles ( $\text{time} \times \text{height}$ ) from the model data, using a modified COSP lidar simulator to perform radiative transfer calculations, calibrating and resampling the observed attenuated volume backscattering coefficient to a common resolution, and conducting similar cloud detection on both the simulated and observed attenuated volume backscattering coefficient (Kuma et al., 2021b).

Aside from these new evaluation techniques, a number of statistical methods have been applied to understand the contribution of clouds to the model radiation biases. Williams and Webb (2009) used a cloud clustering approach to establish cloud regimes in models and compared them with satellite observations, showing a positive bias of shortwave cloud radiative effect in models. Field et al. (2011) utilized the cyclone compositing method to illustrate the underestimation of the TOA reflected shortwave radiation on the cold-air side of cyclones in models. These two techniques were combined by Bodas-Salcedo et al. (2014) to relate cloud regimes and radiative biases to different climatic conditions. It was observed that the cold-air side of the cyclone composite is where the majority of model biases appear, and they mostly occur in the midlevel cloud regime (Bodas-Salcedo et al., 2014).

By incorporating the observational simulators and statistical analysis, climate models' outputs can be assessed against those observations. From previous research on the evaluation of cloud property simulations in models, it can be summarized that, over the SO region, the simulated low-level cloud fractions tend to be lower than both satellite observations (Trenberth and Fasullo, 2010; Bodas-Salcedo et al., 2012; Franklin et al., 2013) and surface-based observations (Protat et al., 2017; Klekociuk et al., 2020; Wang et al., 2020). However, discrepancies do exist between surface and satellite observations due to limitations of near-surface cloud retrievals of satellites.

In the context of widespread supercooled liquid clouds (SLCs), the underestimation of liquid water content in the clouds causes less reflective clouds and consequently less reflected shortwave radiation in the model at the TOA (Hu et al., 2010; Bodas-Salcedo et al., 2016). Additionally, the poor representations of cloud feedbacks attributed to the reduction in low cloud coverage and water content lead to higher climate sensitivity in the Coupled Model Intercomparison Project Phase 6 (CMIP6) compared to the previous version (Zelinka et al., 2020; Schuddeboom and McDonald, 2021; Kuma et al., 2023). Failure to accurately simulate physical properties of clouds in climate models emphasizes the necessity to use a variety of observational datasets to fully evaluate the models and correct biases through modifying the simulation of cloud fraction, cloud types, and cloud thermodynamic phases.

Surface-based observations and satellite products are two main types of datasets used to assess the model's performance. Numerous satellite-based evaluations have been previously conducted (Bodas-Salcedo et al., 2012, 2014, 2016; Luo et al., 2016), including for the Australian Community Climate and Earth System Simulator (ACCESS) model (Fiddes et al., 2018, 2022). Tansey et al. (2022) examined surface precipitation measurements during Macquarie Island Cloud and Radiation Experiment (MICRE) and compared them with data from CloudSat, revealing several notable differences attributable to satellite instrument sensitivities and

algorithm structure. This indicates the limitations of satellites in observing low-level clouds over the SO, which serves as a strong motivation for utilizing ground-based observations to calibrate satellite products. Nonetheless, ground-based observations in the SO and Antarctica remain limited due to the harsh atmospheric environment and lack of remote sites for measurements (Lawson and Gettelman, 2014), leading to less advanced model evaluation techniques than for the Northern Hemisphere. The parameterizations of models have not been comprehensively developed or tuned for the SO region, on account of the paucity of comparable field observations and suitable tools that can allow one-to-one comparison between models and observations (McFarquhar et al., 2021; Kuma et al., 2021b). In recent years, several campaigns have been conducted to collect cloud properties over the SO (Protat et al., 2017; McFarquhar et al., 2021; Kremser et al., 2021). Using these observational data to test climate models with the latest simulators and statistical analysis, as well as calibrate satellite data, remains a critical task.

In this work, we evaluated the capability of ACCESS Atmosphere-only Model version 2 (AM2) to simulate the downwelling surface radiation, cloud radiative effect, and limited cloud properties. Performance of the Cloud and the Earth's Radiant Energy System (CERES) product in reproducing surface radiation and cloud radiative effect was also assessed. The campaign described by McFarquhar et al. (2021) and Tansey et al. (2022) at Macquarie Island was used as the observational dataset for comparison. Furthermore, the ALCF product was used to explore the connection of cloud occurrence and radiative biases in the ACCESS-AM2 model compared with ceilometers for the first time.

The structure of this paper is organized as follows: Sect. 2 describes the data and methods used in the study, Sect. 3 evaluates the surface radiative bias in the ACCESS-AM2 model and CERES product, Sect. 4 presents the distribution of cloud fraction and explores the relationship between cloud fraction and radiative bias in the ACCESS-AM2 model, Sect. 5 examines the histograms of cloud occurrence using the ALCF and investigates the link between cloud occurrence and radiative bias in the ACCESS-AM2 model, and Sect. 6 summarizes the results.

## 2 Data and methods

### 2.1 Overview of ground-based observations

The observational data used in this paper originated from the Macquarie Island Cloud and Radiation Experiment (MICRE), conducted by the United States Department of Energy (DOE) Atmospheric Radiation Measurement (ARM) program, the Bureau of Meteorology (BoM), and the Australian Antarctic Division (AAD), between March 2016 and March 2018. Located at 54.5° S, 158.9° E, and with an altitude of 6 m (Fig. 1a), the year-round AAD research station at Macquarie Island supports a range of scientific activities

and has a long history of surface meteorology observations (Wang et al., 2015). The primary goal of MICRE was to gather surface-based measurements of radiation, precipitation, boundary layer (BL) clouds, and aerosol characteristics in order to evaluate satellite products and improve understanding of diurnal and seasonal fluctuations, particularly in terms of BL cloud vertical structure over the SO (McFarquhar et al., 2021). The data collected during the campaign include downwelling surface radiation fluxes, precipitation rates, and ceilometer backscatter measurements along with standard meteorological observations.

### 2.2 Instrumentation

Instruments involved in the analysis of cloud radiative bias include a set of AAD broadband radiometers, which measure downwelling surface shortwave (SW) and longwave (LW) radiation fluxes; a ceilometer from the University of Canterbury to determine cloud base height (CBH); and an AAD all-sky cloud camera to record cloud fraction. Measurements of all instruments cover the period from 5 April 2016 to 6 March 2018.

#### 2.2.1 Radiometers

Both a Kipp & Zonen CMP21 pyranometer (SW) and a Kipp & Zonen CGR4 pyrgeometer (LW) which are sensitive over 285–2800 nm and 4.5–42 µm, respectively, were used to collect radiation data (Fig. 1b). The sensors have a time resolution of 1 min, and results were recorded as means and standard deviations for each of the 600 individual readings of output voltage at 1 min interval and logged on a Campbell Scientific CR3000 data logger.

The LW radiation fluxes ( $\text{W m}^{-2}$ ) were calculated using

$$L_d = \frac{U_{\text{emf}}}{S_L} + 5.67 \times 10^{-8} \cdot T_b^4, \quad (1)$$

where  $U_{\text{emf}}$  is the pyrgeometer output voltage ( $\mu\text{V}$ ),  $S_L$  is the pyrgeometer sensitivity ( $\mu\text{V} (\text{W m}^{-2})^{-1}$ ), and  $T_b$  is the thermistor temperature (K) of the pyrgeometer. The temperature (K) was calculated using

$$T_b = \left( \alpha + [\beta \cdot \ln(R) + \gamma \cdot (\ln(R))^3] \right)^{-1}, \quad (2)$$

where  $R$  is the resistance ( $\Omega$ ) and  $\alpha$  ( $1.0295 \times 10^{-3}$ ),  $\beta$  ( $2.391 \times 10^{-4}$ ), and  $\gamma$  ( $1.568 \times 10^{-7}$ ) are calibration coefficients from the Kipp & Zonen calibration certificate.

The SW radiation fluxes ( $\text{W m}^{-2}$ ) were calculated using

$$S_d = \frac{U_{\text{emf}}}{S_S}, \quad (3)$$

where  $U_{\text{emf}}$  is the pyranometer output voltage ( $\mu\text{V}$ ) and  $S_S$  is the pyranometer sensitivity ( $\mu\text{V} (\text{W m}^{-2})^{-1}$ ).

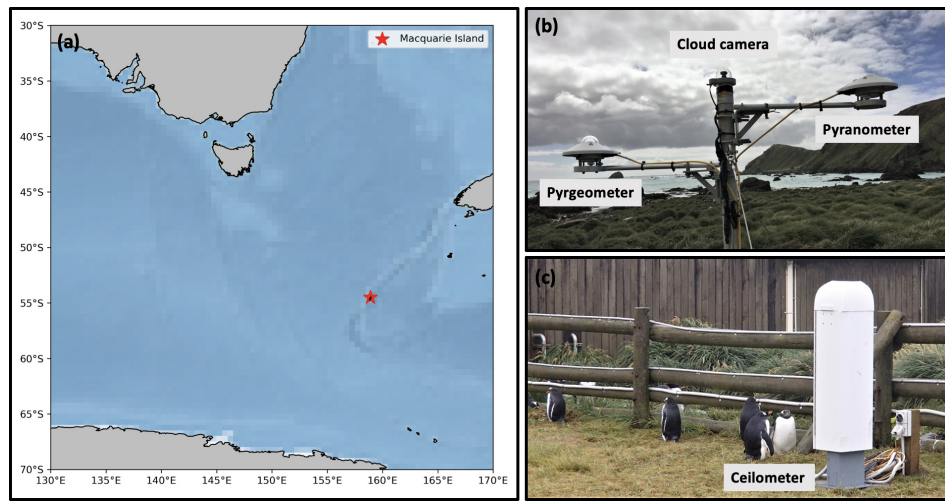


**Figure 1.** (a) Location of Macquarie Island ( $54.5^{\circ}$  S,  $158.9^{\circ}$  E). The blue color scale represents the bathymetry of oceans. (b) Photo of cloud camera (on top of the mast), pyranometer (on the arm to the right), and pyrgeometer (on the arm to the left) installed in the Clean Air Lab enclosure (credit: Andrew Klekociuk, Australian Antarctic Division). (c) Photo of the Vaisala CL51 ceilometer installed in the Bureau of Meteorology lab, about 200 m away from cloud camera and radiometers (credit: Jeff Aquilina, Bureau of Meteorology).

The uncertainty in pyranometer measurements is derived from the sensitivity ( $\pm 0.11 \mu\text{V} (\text{W m}^{-2})^{-1}$ ), and the uncertainty of the pyrgeometer is derived from the combination of sensitivity ( $\pm 0.30 \mu\text{V} (\text{W m}^{-2})^{-1}$ ) and temperature measurements ( $\pm 0.11 \text{ K}$ ). The radiometers were validated against a separate set of radiometers that were part of the ARM deployment at Macquarie Island (see Appendix A). The two independent datasets were found to be comparable within 2 % for the SW and 5 % for the LW, which are within the uncertainty of the instrumentation.

Both the pyranometer and pyrgeometer sensors were changed on 19 March 2017. Prior to this date the sensitivities ( $S_S$  and  $S_L$ ) were  $8.89$  and  $13.01 \mu\text{V} (\text{W m}^{-2})^{-1}$ , and after this date they were  $9.23$  and  $9.07 \mu\text{V} (\text{W m}^{-2})^{-1}$ . From Eq. (1), the pyrgeometer requires a temperature measurement to calculate the radiation flux. This is nominally obtained from a thermistor aboard the sensor; however, a cable fault between 5 July 2016 at 14:37 UT and 23 November 2016 at 02:22 UT affected the thermistor resistance and consequently the measured temperature. Over this interval temperatures were substituted with those obtained from a similar thermistor aboard the pyranometer. Temperatures differences were within 1 % between the two thermistors on average. Prior to 23 May 2017, the dataset was recorded with the Campbell logger default data type FP2, which has a range limit of  $-7999$  to  $7999 \mu\text{V}$ . This inadvertently clipped the SW (pyranometer) data that exceeded  $7999/8.89 = \sim 900 \text{ W m}^{-2}$  before 19 March 2017 and  $7999/9.23 = \sim 867 \text{ W m}^{-2}$  between 19 March and 23 May 2017. The LW (pyrgeometer) data were unaffected by this effect. The limited clipped points that accounted for approximately 3 % of the whole dataset were removed. This was corrected to an IEEE 4 B data type on

23 May 2017, which has a  $\pm 2.1^{5}e^9$  range limit and 1 bit resolution that covered all levels of voltage output by the sensor. Additionally, 9 d of data, which accounted for approximately 1 % of the whole dataset, were removed because of too few data points on those days to statically calculate a daily average.

## 2.2.2 Ceilometer

A Vaisala CL51 ceilometer, which is a vertically pointed near-infrared lidar with a regular vertical resolution of 10 m that operates at a wavelength of 910 nm ( $\pm 10 \text{ nm}$ ) up to a range of 15.4 km, was employed to detect attenuated backscatter (Fig. 1c). A two-dimensional (time  $\times$  range) range-corrected attenuated backscatter profile was sampled every 6 s as the primary output (Klekociuk et al., 2020). The ceilometer observations were sub-sampled to 5 min time resolution and 50 m vertical resolution by averaging multiple columns and bins through the ALCF (Kuma et al., 2020). Columns and bins here are, respectively, time and vertical intervals of the backscatter profile. Information on CBH, precipitation, and at times boundary layer height can be obtained from the backscatter profile using detection algorithms. Fog can be observed in the backscatter profiles as well. However, there are limitations to the capabilities of a ceilometer. Cloud tops and upper cloud layers are typically not visible in the backscatter profile due to the absorption of laser energy by thick clouds. As a result, the instrument is best suited for monitoring low-level clouds, although it may also be used to observe mid- to high-level clouds in the absence of low-level clouds (Klekociuk et al., 2020). Moreover, the signal and noise properties of the Vaisala CL51 ceilometer were investigated by Kotthaus et al. (2016), and a system-

atic bias was noted in the attenuated backscatter recorded by the instrument, which is determined by the internal calibration. Calibration of the instrument is achieved by scaling the backscatter signal to match the observed lidar ratio with the theoretical value (O'Connor et al., 2004).

During the selected period for conducting the radiation–cloud occurrence analysis in Sect. 5, which spanned from September 2017 to February 2018, approximately 6.7 % of the ceilometer data were excluded due to poor quality.

### 2.2.3 All-sky cloud camera

For the cloud fraction (CF) analysis, color images were taken at 1 min intervals with an all-sky camera (Fig. 1b). Both “all-sky” and “zenith” regions of interest (ROIs) were included in the data processing, which comprised most of the unobstructed sky and an 8° radius field at the zenith, respectively. Based on a color charge-coupled device (CCD) sensor, the camera contains a three-element 1.24 mm F2.8 lens that gives a 190° hemispherical “fisheye” field of view (FoV) to determine cloud distribution (Klekociuk et al., 2020; Wang et al., 2020). In terms of FoV of the cloud camera, it covered an area of 52 km in diameter at 4.5 km altitude. For each image captured during the day (solar elevation > 5°), a modified version of the blue-red pixel ratio and differencing algorithms were employed to distinguish clear-sky and cloudy-sky pixels. Cumulative pixel counts, previously applied in several studies, were used to establish a CF (Li et al., 2011; Ghonima et al., 2012; Yabuki et al., 2014). For the pixel ratio algorithm (BdR – blue channel divided by red channel), a threshold of 1.3 was applied to the 8 bit (0–255) blue/red components to differentiate blue (clear-sky) pixels. For the pixel differencing algorithm (BmR – blue channel minus red channel), a threshold of 30 was applied to 8 bit (0–255) blue-red components to differentiate blue (clear-sky) pixels. The cloud camera dataset was organized to align with the available radiometer dataset, ensuring that the measurement of the CF could be directly linked with radiation data.

## 2.3 Algorithms for cloud radiative effect and clear-sky radiation

### 2.3.1 Cloud radiative effect (CRE)

The cloud radiative effect (CRE) is defined as the influence of clouds on total radiation budget, computed from the difference in SW radiation and LW radiation between all-sky and clear-sky conditions (Wang et al., 2020). According to Shupe and Intrieri (2004) and Dommenget and Flöter (2011), the CRE is defined as

$$\text{CRE}(\theta) = (1 - \alpha) \cdot (S(\theta) - S_0(\theta)) + \varepsilon \cdot (L(\theta) - L_0(\theta)), \quad (4)$$

which can be divided into shortwave cloud radiative effect ( $\text{CRE}_{\text{SW}}$ ),

$$\text{CRE}_{\text{SW}}(\theta) = (1 - \alpha) \cdot (S(\theta) - S_0(\theta)), \quad (5)$$

and longwave cloud radiative effect ( $\text{CRE}_{\text{LW}}$ ),

$$\text{CRE}_{\text{LW}}(\theta) = \varepsilon \cdot (L(\theta) - L_0(\theta)), \quad (6)$$

where  $\alpha$  is the surface SW albedo;  $\varepsilon$  is the LW surface emissivity;  $\theta$  is the solar zenith angle;  $S(\theta)$  and  $S_0(\theta)$  are, respectively, the downwelling surface SW radiation in all-sky and clear-sky conditions; and  $L(\theta)$  and  $L_0(\theta)$  are, respectively, the downwelling surface LW radiation in all-sky and clear-sky conditions. In this analysis,  $\alpha = 0.055$  and  $\varepsilon = 0.97$  were used to permit comparisons with earlier investigations (Fairall et al., 2008; Protat et al., 2017; Klekociuk et al., 2020).

### 2.3.2 Clear-sky radiation

Along with the measured SW and LW radiation under all-sky conditions, estimating the clear-sky radiation field is necessary to obtain the values of  $S_0(\theta)$  and  $L_0(\theta)$  before calculating the CRE using Eq. (4). Macquarie Island is almost constantly covered by clouds, where only 0.6 % of time was classified as clear sky by the all-sky camera. The limited observed clear-sky conditions meant we were unable to satisfactorily validate clear-sky models such as the SW clear-sky model by Corripio (2003) and the LW clear-sky model by Idso (1981). Both of these clear-sky models, upon comparison to the ACCESS-AM2 and satellite products, showed large biases, even using the parameters tuned for the SO provided by Wang et al. (2020).

With this in mind, we have used the downwelling surface clear-sky radiation fields from the European Center for Medium-range Weather Forecasting (ECMWF) Reanalysis 5 (ERA5) (Hersbach et al., 2020) for calculating cloud radiative effects. Assimilated measurements from different microwave sounders provide information on brightness temperatures and humidity to derive the clear-sky radiation in ERA5 (Hersbach et al., 2020). The ERA5 clear-sky fields have been used to validate other clear-sky models, such as in Shakespeare and Roderick (2021). The ACCESS-AM2 and CERES products both take into account ERA5 atmospheric properties, and hence each of these three products showed minimal differences. In this way we are able to limit introduced biases due to inaccurate clear-sky fields. We suggest that further efforts are needed to validate clear-sky models for the SO.

## 2.4 ACCESS-AM2

ACCESS-AM2 uses the same configuration as the ACCESS-CM2 (coupled model) without the ocean. The atmospheric component of ACCESS-AM2 is based on the UK Met Office's (UKMO) Unified Model (UM) version 10.6 Global Atmosphere (GA) 7.1 (Walters et al., 2019), with the Community Atmosphere Biosphere Land Exchange (CABLE) version 2.5 land surface model (Bi et al., 2020). The model has been operated globally at N96 resolution (approximately

1.25° latitude by 1.875° longitude) with 85 vertical levels (Bi et al., 2020; Bodman et al., 2020). Model output has been saved as daily means from April 2016 to March 2018 and limited hourly instantaneous output from September 2017 to February 2018 to coincide with three other campaigns described in McFarquhar et al. (2021) besides MICRE.

The ACCESS-AM2 model is configured for the Atmospheric Model Intercomparison Project (AMIP) simulations, contributing to the Coupled Model Intercomparison Project Phase 6 (CMIP6) experiments (Eyring et al., 2016). The model used in this study is nudged to ERA5 (Hersbach et al., 2020). The horizontal wind and temperature in the free troposphere and stratosphere were nudged at every dynamical time step using reanalysis fields and updated every 3 h (Fiddes et al., 2022). Sea surface temperatures (SSTs) and sea ice concentrations (SICs) are derived in accordance with the input4MIPS database and updated to cover the time period of this simulation (Hurrell et al., 2008). Solar forcing, greenhouse gases (GHGs), volcanic aerosol optical depth, and ozone are prescribed in the ACCESS-AM2 following the CMIP6 AMIP model configuration (Eyring et al., 2016).

Of interest to this study, the ACCESS-AM2 model uses the Suite Of Community RAdiative Transfer codes based on Edwards and Slingo (SOCRATES) (Edwards and Slingo, 1996) and Wilson et al.'s (2008) prognostic CF and condensate cloud scheme, which includes large-scale as well as convective clouds. For comparison with the observational data, the radiation and prognostic CF in the model was linearly interpolated to the point nearest to Macquarie Island (54.5° S, 158.9° E). Additional details associated more generally with the ACCESS-AM2 model can be found in Bodman et al. (2020), and these specific simulations are detailed in Fiddes et al. (2022).

## 2.5 CERES SYN 1° dataset

The CERES project provides satellite-based observations of global clouds and radiation budgets. CERES instruments measure SW broadband radiances in 0.3–5 µm and LW broadband radiances in 5–200 µm (<https://ceres.larc.nasa.gov/instruments>, last access: 21 January 2023). The CERES Synoptic TOA and downwelling surface fluxes and clouds (SYN) 1° product calculates hourly, 3-hourly, daily, and monthly surface SW and LW fluxes using cloud and aerosol properties derived from a variety of sources (Rutan et al., 2015). In this study we examine the daily CERES SYN 1° Edition 4A product by linearly interpolating to the point nearest to Macquarie Island (54.5° S, 158.9° E) from April 2016 to March 2018, for consistency with the observational data.

## 2.6 ALCF

The ALCF is an open-source command line tool that processes ALC data and compares them to GCMs, NWP mod-

els, and reanalysis. It conducts the required steps to model the ALC attenuated volume backscattering coefficient by extracting cloud liquid and ice mixing ratios, cloud fraction, and thermodynamic data from the model. Additionally, the ALCF transforms the observed raw ALC attenuated volume backscattering coefficient profiles to make them comparable with the simulated profiles (Kuma et al., 2021b).

For the model data, the ALCF first extracts two-dimensional cloud liquid and ice content profiles at the survey area and then uses the Subgrid Cloud Overlap Profile Sampler (SCOPS) to generate 10 random subcolumns for each profile to detect clouds in the model (Chepfer et al., 2008). The default setting for generating cloud overlap is maximum-random overlap assumption, which assumes neighboring layers with non-zero CF are fully overlapped, while layers separated by zero CF are randomly overlapped. The same sampling rate (5 min) and vertical bins (50 m) were used in lidar simulator to make the model and observations comparable. The attenuated volume backscattering coefficient profiles are then simulated for 10 subcolumns based on the COSP lidar simulator. Subsequently, the ALCF resamples the observational profiles to increase the signal-to-noise ratio, subtracts the noise, calculates the lidar ratio, applies an absolute calibration, and uses a cloud detection algorithm to calculate cloud mask and CBH for both simulated and observational data. A threshold of  $6 \times 10^{-6} \text{ m}^{-1} \text{ sr}^{-1}$  for backscattering coefficient is applied to identify cloud mask after removing 5 standard deviations of range-scaled noise. This value was found to be a good compromise between false detection and misses of cloud at Macquarie Island, where the boundary layer aerosol is prevalent, after testing different threshold values. This step is important to make the simulated and observed backscattering coefficient profiles comparable. Next, the statistical summary including the CF, cloud frequency of occurrence (CFO), and attenuated volume backscattering coefficient histograms is derived. The CFO is calculated for each height level by counting the number of bins which have a positive cloud mask divided by the total number of columns in the time range. The total CF is calculated by counting the number of columns which have at least one cloudy bin, divided by the total number of columns in the time range. For the ceilometer data, the ALCF applies the same operations as the model but starts from the denoised step. Plots of cloud occurrence representing the CBH and attenuated volume backscattering histogram are generated from the ALCF code. More information about this framework can be found in Kuma et al. (2021b).

Several limitations exist within the ALCF that can cause uncertainties (Kuma et al., 2021b). Firstly, the accuracy of the CL31 and CL51 ceilometers' calibration may be impacted by the absorption of water vapor at 910 nm, which can limit the precision of their comparison. However, it is improbable that the calculated cloud masks will be significantly influenced due to the high backscattering caused by clouds. Secondly, precipitation and aerosol are not currently

implemented in the simulator. The cloud detection algorithm typically identifies observed precipitation as “cloud”, whereas the simulated profile does not show any backscattering in the area where precipitation is occurring. Finally, the ALCs also encounter several measurement limitations. Specifically, inadequate overlap, dead time, and after-pulse corrections often yield sub-optimal outcomes at close range. Semi-automated methods include calculating the distribution of integrated attenuated volume backscattering coefficient by analyzing the height where maximum backscattering occurs.

The ALCF was operated from September 2017 to February 2018 to correspond with the hourly ACCESS-AM2 output in this study. The cloud occurrence in the ALCF output was primarily used to investigate the relationship between the cloud radiative bias and the representation of cloud occurrence in the model.

### 3 Surface radiative biases

#### 3.1 All-sky and clear-sky surface radiation biases

Figure 2 shows the time series of daily averaged surface SW and LW radiation fluxes at Macquarie Island from April 2016 to March 2018 based on the surface radiometer (dotted black line), ACCESS-AM2 model (red line), and CERES satellite product (blue line). During this 2-year period, the SW radiation fluxes in the upper panel present a clear annual cycle, reaching the peak in austral summer (DJF) of around  $250 \text{ W m}^{-2}$ . This annual cycle is also found in the magnitude of the SW fluctuations, with the smallest amplitude variability in winter and the largest amplitudes in summer. The surface SW radiation fluxes simulated by ACCESS-AM2 model and CERES align with observations regarding the  $R^2$  values of 0.79 and 0.93, respectively (Fig. 2a). For LW radiation fluxes in the lower panel, some variation is visible with lower downwelling LW flux in winter than in summer, which would be expected since the clouds and atmosphere are colder in winter and thus radiating less LW radiation to the surface. The magnitude of LW fluxes varies mainly between 250 and  $350 \text{ W m}^{-2}$ , with a lower variability than SW fluxes. For the LW radiation fluxes, with the exception of winter (JJA) when the CERES exhibits a clear underestimation, the model and satellite conform to the observations well.

The model and satellite product, respectively, show Pearson correlations of SW radiation fluxes of 0.92 (ACCESS-AM2) and 0.98 (CERES) compared to the observations, with the periodicity of SW radiation enhancing these results. After monthly detrending, the correlations decrease to 0.72 and 0.94, suggesting a good performance by the model and excellent performance by the satellite product. The LW correlation between observation and ACCESS-AM2 model remains unchanged at 0.80 before and after eliminating monthly effects. However, this correlation rises from 0.82 to 0.86 between observation and satellite, possibly by artificially removing the wintertime low bias. The differing capability of model and

satellite to simulate observed surface SW and LW demonstrates the necessity for validation of satellite products in reproducing surface radiation fluxes, including the radiative retrieval algorithms, before utilizing them to evaluate climate models.

Table 1 displays the total and seasonal averages of surface SW and LW radiation fluxes calculated using daily means under all-sky and modeled clear-sky conditions as well as their biases in observational, model, and satellite datasets. Figure 3 shows the seasonal distribution of SW and LW radiation fluxes in all-sky and clear-sky conditions. For the ACCESS-AM2 model, annually there is an overestimation of  $+9.5 \pm 33.5 \text{ W m}^{-2}$  in SW fluxes and a small underestimation of  $-2.3 \pm 13.5 \text{ W m}^{-2}$  in LW fluxes in cloudy conditions (Table 1). The number following the  $\pm$  sign indicates the daily standard deviation but not the confidence interval as illustrated in the bolded brackets of the table. The overestimation of SW radiation in the model is pronounced in spring and becomes more so in summer, during which season the mean SW radiation simulated by the model is  $+25.0 \pm 48.0 \text{ W m}^{-2}$  higher than the observations. As illustrated in Fig. 3a, the model's distribution (blue) exhibits a large shift to higher radiation fluxes relative to the observation (red) in the summer. The differences for LW radiation fluxes in the model are minor throughout all seasons, reaching  $-4 \text{ W m}^{-2}$  in autumn, with smaller differences in all other seasons. The CERES product has an overestimation of  $+8.0 \pm 18.0 \text{ W m}^{-2}$  in SW radiation fluxes and a large underestimation of  $-12.1 \pm 12.2 \text{ W m}^{-2}$  in LW radiation fluxes in all-sky conditions. Similar to ACCESS-AM2, the SW radiation biases of the satellite product are greater in the spring and summer than in the autumn and winter. From Fig. 3a, the satellite's distribution (green) shows a large shift to higher value in comparison to the observation (red) in the summer, which is comparable to the model. The LW radiation biases of the satellite are much larger than those of the model, with the highest biases occurring in autumn and winter. This is especially evident in Fig. 3b, where there is a very significant shift to smaller radiation fluxes in the distribution of the satellite data compared to the observation and model.

When it comes to simulated clear-sky conditions, the ACCESS-AM2 surface shortwave (SWcs) and longwave (LWcs) radiation fluxes were found to have biases of  $-2.3 \pm 3.7$  and  $+4.5 \pm 5.3 \text{ W m}^{-2}$  in total (Table 1), when compared to the ERA5 clear-sky product. Non-significant negative SWcs biases in the model are consistent across all seasons and the distribution of SWcs of ACCESS-AM2 and ERA5 fit well (Fig. 3c). The biases for LWcs fluxes in the ACCESS-AM2 model are statistically significant and more notable in spring and summer (Fig. 3d). The satellite's LW biases and seasonal distributions in clear-sky conditions are similar to ACCESS-AM2 when comparing with ERA5, while the SW biases are more negligible (Fig. 3c, d). The significant differences of LWcs in model and satellite compared to ERA5 highlight the need for more validation and development of

**Table 1.** Annual and seasonal means of downwelling SW and LW fluxes in all-sky and clear-sky conditions.

$\text{W m}^{-2}$	Observation	ACCESS-AM2	Bias (ACCESS-AM2)	CERES	Bias (CERES)
<b>Annual</b>					
SW mean	95.9 [76.3]	105.4 [83.4]	<b>9.5 [4.3]*</b>	103.9 [81.4]	<b>8.0 [4.2]*</b>
SWcs mean	189.5 [127.9] (ERA5)	187.2 [127.3]	<b>-2.3 [6.8]</b>	189.2 [127.6]	<b>-0.3 [6.8]</b>
LW mean	314.0 [21.8]	311.7 [19.8]	<b>-2.3 [1.1]*</b>	301.9 [16.6]	<b>-12.1 [1.0]***</b>
LWcs mean	251.0 [14.8] (ERA5)	255.5 [15.6]	<b>4.5 [0.8]***</b>	255.3 [13.0]	<b>4.3 [0.7]***</b>
<b>Summer (DJF)</b>					
SW mean	171.5 [64.3]	196.5 [60.5]	<b>25.0 [6.6]***</b>	191.3 [60.9]	<b>19.8 [6.6]**</b>
SWcs mean	341.5 [43.5] (ERA5)	339.2 [42.6]	<b>-2.3 [4.6]</b>	340.9 [43.5]	<b>-0.6 [4.6]</b>
LW mean	320.7 [21.0]	318.0 [19.7]	<b>-2.7 [2.2]</b>	312.7 [14.6]	<b>-8.0 [1.9]***</b>
LWcs mean	259.7 [12.2] (ERA5)	264.8 [13.1]	<b>5.1 [1.3]***</b>	262.5 [10.7]	<b>2.8 [1.2]*</b>
<b>Autumn (MAM)</b>					
SW mean	51.9 [37.3]	52.3 [33.0]	<b>0.4 [4.1]</b>	52.9 [35.9]	<b>1.0 [4.2]</b>
SWcs mean	105.7 [59.6] (ERA5)	103.8 [59.6]	<b>-1.9 [6.9]</b>	105.3 [60.0]	<b>-0.4 [6.9]</b>
LW mean	317.6 [20.5]	314.0 [19.4]	<b>-3.6 [2.3]</b>	302.9 [14.9]	<b>-14.7 [2.1]***</b>
LWcs mean	254.3 [14.2] (ERA5)	257.6 [14.4]	<b>3.3 [1.7]*</b>	258.8 [12.4]	<b>4.5 [1.5]**</b>
<b>Winter (JJA)</b>					
SW mean	26.8 [17.6]	24.6 [16.3]	<b>-2.2 [1.8]</b>	27.1 [16.9]	<b>0.3 [1.8]</b>
SWcs mean	52.5 [25.5] (ERA5)	50.7 [25.1]	<b>-1.8 [2.6]</b>	52.1 [25.5]	<b>-0.4 [2.7]</b>
LW mean	307.3 [21.5]	307.2 [17.8]	<b>-0.1 [2.1]</b>	290.5 [12.7]	<b>-16.8 [1.8]***</b>
LWcs mean	242.7 [13.4] (ERA5)	246.9 [14.3]	<b>4.2 [1.4]**</b>	248.6 [12.1]	<b>5.9 [1.3]***</b>
<b>Spring (SON)</b>					
SW mean	127.8 [60.8]	141.1 [59.3]	<b>13.3 [6.3]*</b>	137.5 [60.0]	<b>9.7 [6.3]</b>
SWcs mean	249.6 [77.2] (ERA5)	246.2 [76.7]	<b>-3.4 [8.1]</b>	249.3 [76.8]	<b>-0.3 [8.1]</b>
LW mean	311.2 [21.6]	308.4 [20.4]	<b>-2.8 [2.2]</b>	302.1 [15.8]	<b>-9.1 [2.0]***</b>
LWcs mean	248.0 [13.2] (ERA5)	253.1 [14.9]	<b>5.1 [1.5]***</b>	252.0 [11.7]	<b>4.0 [1.3]**</b>

All values have units of watts per square meter ( $\text{W m}^{-2}$ ). The bolded biases were calculated based on mean surface fluxes (e.g., ACCESS-AM2 – observation, CERES – observation). When present, brackets “[ ]” show the day-to-day standard deviation, while bolded brackets show the standard error of the mean difference, which reflects if the biases can be considered significant at a certain confidence interval. The biases with “\*\*” mean the  $p$  value  $< 0.1$ , biases with “\*\*\*” mean the  $p$  value  $< 0.01$ , and biases with “\*\*\*\*” mean the  $p$  value  $< 0.001$ .

especially the LWcs models. The SWcs models show smaller and insignificant biases, indicating less uncertainty.

After quantifying the average biases and the seasonal distributions of radiation data from the ACCESS-AM2 model and the satellite product, we can now further explore the causes of these biases. Numerous studies have corroborated the overestimation of surface SW radiation in climate models, reaching a maximum in summer (Trenberth and Fasullo, 2010; Franklin et al., 2013; Mason et al., 2015; Luo et al., 2016). The larger quantity of solar radiation in the spring and summer compared to the autumn and winter causes the cloud bias in these periods to have a larger impact on the radiative balance (Luo et al., 2016; Fiddes et al., 2022). The underestimated CF and liquid water content in the model are believed to be the major explanation for this overestimation (Mason et al., 2015; Luo et al., 2016; Kuma et al., 2020). “Too few and too bright” low-level clouds were identified as the cause of this SW bias in CMIP5 models (Nam et al., 2012; Wall et al., 2017). Nevertheless, more recently, Schuddeboom and Mc-

Donald (2021) discovered the exact contrasting result in the CMIP6 simulations, which demonstrates the importance of prioritizing the low-level cloud simulation to enhance the SW radiative balance over the SO. The LW radiation biases can be expected to also originate largely from cloud occurrence and cloud microphysics biases and to a lesser extent atmospheric temperature and humidity biases (Wild et al., 2001). The physical reason is a high emissivity of clouds compared to the atmosphere, so the surface is more radiatively coupled to clouds as opposed to the thermally very cold space. For downwelling surface radiation in clear-sky conditions, Wild et al. (2006) suggest earlier GCMs overestimated SWcs radiation due to a lack of suitable aerosol forcing and an overestimated water vapor absorption. The influence of aerosol in the representation of SWcs radiation in climate models has been confirmed by Ruiz-Arias et al. (2013). Nevertheless, ACCESS has been shown (unpublished) to underestimate radiation-relevant aerosol over the SO, which does not fit with the underestimated SWcs bias here. Significantly, fur-

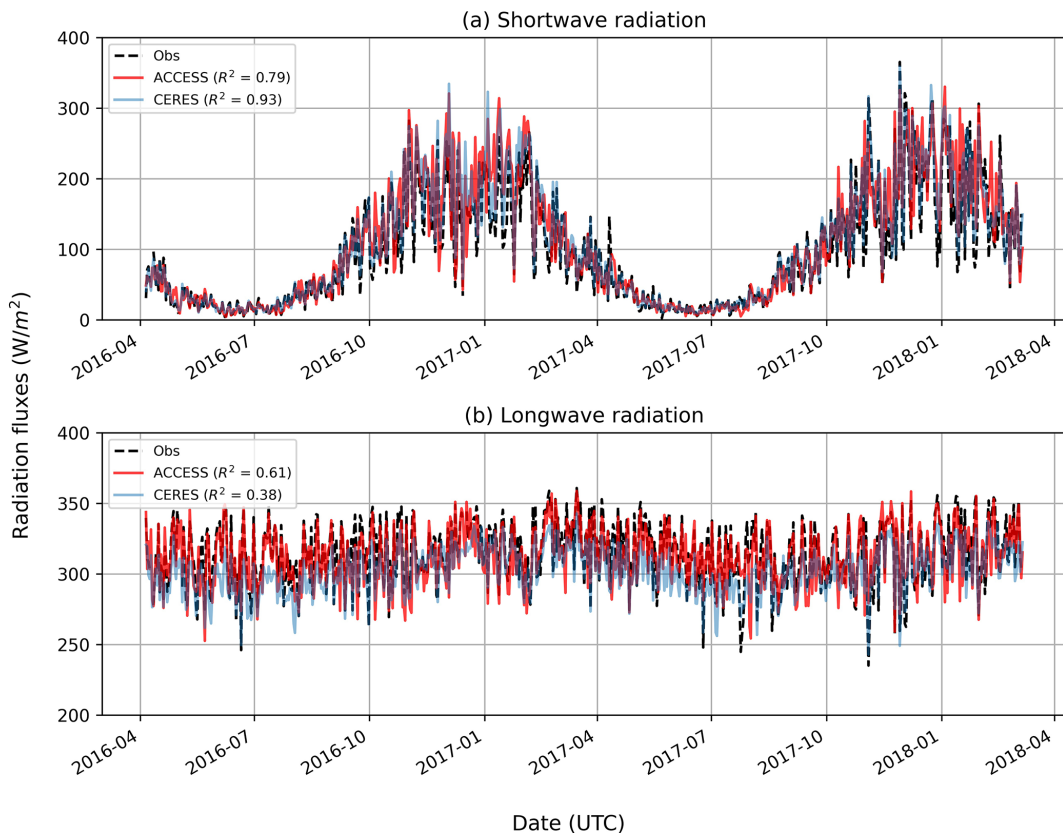


**Figure 2.** Time series of daily means of downwelling surface SW (a) and LW (b) radiation fluxes during MICRE. The dotted black line represents surface observations, the red line represents ACCESS-AM2 outputs, and the blue line represents CERES observations. The coefficient of determination is indicated in the legend.

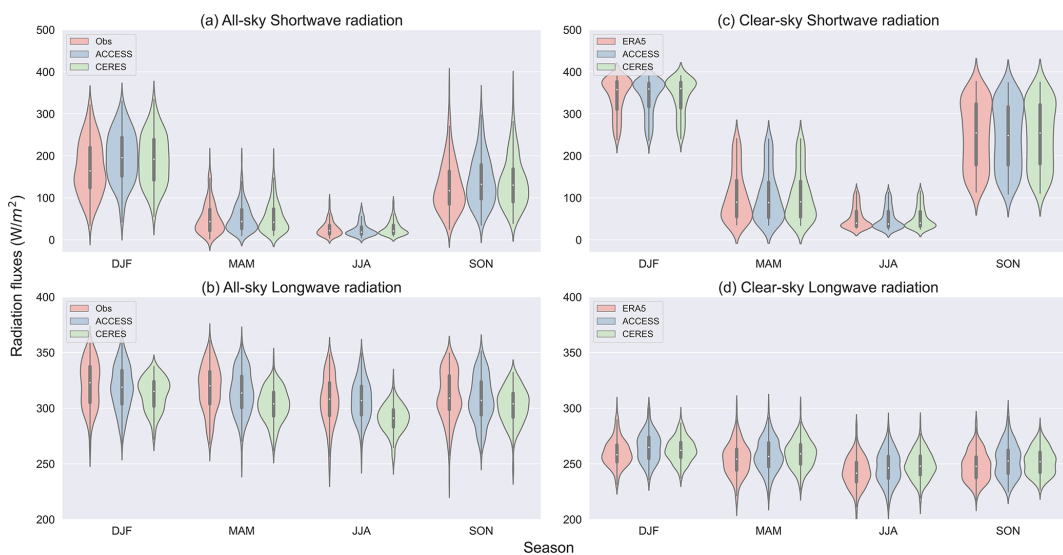


**Figure 3.** Violin plot of seasonal distributions of downwelling surface SW (a, c) and LW (b, d) radiation fluxes in all-sky and clear-sky conditions among surface observations, the ACCESS-AM2 model, and satellite data. The white dot in the middle represents the median, the thick gray bar represents the interquartile range, and the thin gray line represents the rest of the distribution. The width of the violin plot represents the distribution of the radiation value.

ther work needs to be done to understand both aerosol as well as water vapor, which has been understudied over the SO to solve the SWCs biases in the ACCESS-AM2 model. The consistent biases in LWcs could be partially explained by the difference in the humidity profiles and near-surface temperature according to Allan (2000), who evaluated the simulated LWcs against ground-based observations.

For CERES data, non-negligible biases are also present. The SW bias of  $+8.0 \pm 18.0 \text{ W m}^{-2}$  and LW bias of  $-12.1 \pm 12.2 \text{ W m}^{-2}$  are slightly different to the previous study by Hinkelmann and Marchand (2020) in magnitude ( $+10 \text{ W m}^{-2}$  for SW bias and  $-10 \text{ W m}^{-2}$  for LW bias), which used a co-located observational dataset collected by ARM at Macquarie Island. These differences in SW and LW biases are possibly attributed to the different temporal resolution of the CERES SYN product (hourly output used in Hinkelmann and Marchand, 2020, and daily output used in this study) and different interpolation methods to collocate data to Macquarie Island (Hinkelmann and Marchand, 2020, chose the nearest grid that contains Macquarie Island, while this study linearly interpolated data to Macquarie Island). Other factors such as data gaps, sampling uncertainty, calibration offsets, different pyranometers, and local shadowing effects may also contribute to the biases difference. Hinkelmann and Marchand (2020) showed that the LW biases in the CERES were caused by an inaccurately low CBH at night. Non-negligible biases in SW and LW fluxes indicate the importance of evaluating and improving the retrieval algorithms for surface radiation fluxes in satellite data, with larger biases in summer for SW radiation and in winter for LW radiation.

Excellent alignment of SWCs radiation between the satellite and reanalysis is expected given the CERES product uses ERA5 to inform its radiative transfer algorithm. While few studies have been focused on LWcs biases, the biases of similar magnitude for the satellite product and the model suggest that more attention needs to be paid to the clear-sky algorithms, including for the ERA5 parameterization. Once again, we suggest the parameterization of humidity and temperature, and their use in the clear-sky models, must be a point of focus.

Understanding the biases in the respective SW and LW clear-sky biases is an important but often neglected component of understanding the CREs. Here we have shown that while the SWCs biases from ACCESS-AM2 and CERES (using similar meteorology driven by ERA5 and using the same method of calculating the clear-sky fluxes) are very similar, the same cannot be said for the LWcs. These differences, and how they affect the CRE, require further study. Wang et al. (2020) evaluated the cloud radiative effect of ERA5 using ship-based measurements in the SO during three summer seasons. Higher shortwave cloud radiative effect ( $+77 \text{ W m}^{-2}$ ) and lower longwave cloud radiative effect ( $-18 \text{ W m}^{-2}$ ) were detected in ERA5 in all-sky conditions, which are likely attributed to the higher occurrence of clouds over the Southern Ocean compared to what was modeled and

potentially resulting from the higher transmittance of clouds in the ERA5 (Wang et al., 2020). Regarding clear-sky conditions, no notable error was found in the ERA5 LW irradiance, while for SW, the observed values were  $33 \text{ W m}^{-2}$  higher than those predicted by ERA5. More recently, Mallet et al. (2023) found large downwelling SW radiation biases ( $+54 \text{ W m}^{-2}$ ) in the ERA5 compared with 25 years of summertime surface measurements collected from ship and ground stations over the SO. By employing machine learning techniques, cloud cover and relative humidity exhibited a strong contribution to the SW radiation biases. Despite these few studies on ERA5 radiation biases, a limited amount of research has been dedicated to investigating this issue, particularly in relation to clear-sky conditions. We emphasize the importance of using ground-based observations of clear-sky radiation to evaluate the model and satellite, as well as validating the reanalysis product.

After investigating the SW and LW radiation biases of ACCESS-AM2 and CERES in both all-sky and clear-sky conditions, we next assess their capability to reproduce cloud radiative effects.

### 3.2 Surface cloud radiative effect (CRE) biases

The surface cloud radiative effect (CRE) determines the role of clouds in the surface radiation budget (defined in Sect. 2.3). A positive CRE indicates that clouds are warming the surface, while a negative CRE implies a surface cooling.

Figure 4 shows the time series of daily average total CRE,  $\text{CRE}_{\text{SW}}$ , and  $\text{CRE}_{\text{LW}}$  in the three datasets. The time series of total CRE and  $\text{CRE}_{\text{SW}}$  shows an evident annual cycle in which the value is significantly negative in the summer, reduces during autumn, and reaches a minimum value in winter. The  $\text{CRE}_{\text{LW}}$ , similar to the all-sky condition, does not show a clear annual cycle, being stable across the year and ranging from 0 to  $+80 \text{ W m}^{-2}$ .

Table 2 shows the value of the total and seasonal averages and biases of surface total CRE,  $\text{CRE}_{\text{SW}}$ , and  $\text{CRE}_{\text{LW}}$  for surface-based observations, the ACCESS-AM2 model, and CERES product. Figure 5 shows the respective seasonal distributions. For the ACCESS-AM2 model, there is a total CRE of  $-23.0 \pm 58.1 \text{ W m}^{-2}$  contributed by a SW cooling of  $-77.6 \pm 58.8 \text{ W m}^{-2}$  and a LW warming of  $+54.6 \pm 11.7 \text{ W m}^{-2}$  during the 2-year period. A  $\text{CRE}_{\text{SW}}$  bias ( $+11.2 \pm 31.1 \text{ W m}^{-2}$ ) dominates the total CRE bias ( $+4.8 \pm 28.0 \text{ W m}^{-2}$ ). Figure 5a demonstrates that the total CRE bias is largest during the spring and summer. During winter, when total CRE is at the most positive value, the  $\text{CRE}_{\text{LW}}$  has a greater influence on the total CRE than the  $\text{CRE}_{\text{SW}}$ , mainly caused by the biases in clear-sky conditions (Tables 1, 2, and Fig. 5). In comparison to ACCESS-AM2, CERES has a greater total CRE of  $-35.7 \pm 56.3 \text{ W m}^{-2}$ , which is attributed to a larger SW cooling of  $-80.9 \pm 61.6 \text{ W m}^{-2}$  and a smaller LW warming of  $+45.2 \pm 11.5 \text{ W m}^{-2}$ . The seasonal distribution of  $\text{CRE}_{\text{SW}}$  biases in the CERES product follows the

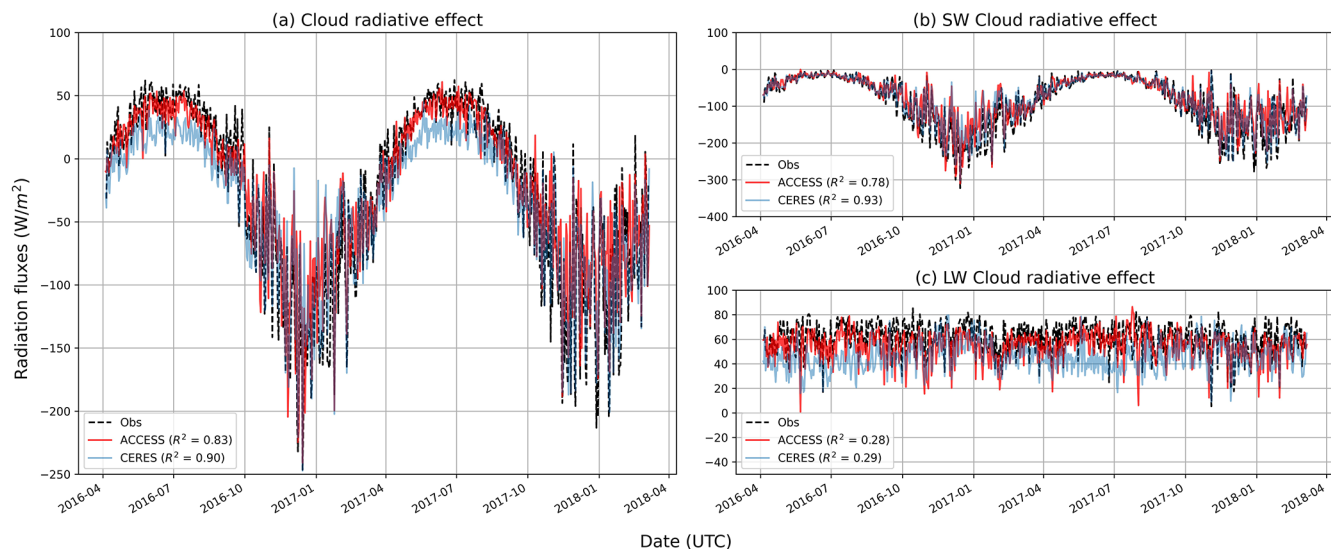


**Figure 4.** Time series of daily means of CRE (a), CRE<sub>SW</sub> (b), and CRE<sub>LW</sub> (c). The dotted black line represents surface observations, the red line represents ACCESS-AM2 outputs, and the blue line represents CERES observations. The coefficient of determination is indicated in the legend.

**Table 2.** Annual and seasonal means of CRE, CRE<sub>SW</sub>, and CRE<sub>LW</sub>.

	W m <sup>-2</sup>	Observation	ACCESS-AM2	Bias (ACCESS-AM2)	CERES	Bias (CERES)
<b>Annual</b>						
CRE mean	-27.8[69.6]	-23.0[58.1]	<b>+4.8 [3.4]</b>		-35.7[56.3]	<b>-7.9 [3.4]*</b>
CRE <sub>SW</sub> mean	-88.8[70.9]	-77.6[58.8]	<b>+11.2 [3.5]**</b>		-80.9[61.6]	<b>+7.9 [3.6]*</b>
CRE <sub>LW</sub> mean	+61.0[12.4]	+54.6[11.7]	<b>-6.4 [0.6]***</b>		+45.2[11.5]	<b>-15.8 [0.6]***</b>
<b>Summer (DJF)</b>						
CRE mean	-101.6[51.0]	-82.9[43.3]	<b>+18.7 [5.0]***</b>		-92.4[46.6]	<b>+9.2 [5.2]*</b>
CRE <sub>SW</sub> mean	-160.2[58.7]	-134.4[50.4]	<b>+25.8 [5.8]***</b>		-140.9[52.1]	<b>+19.3 [5.9]**</b>
CRE <sub>LW</sub> mean	+58.6[12.9]	+51.5[11.4]	<b>-7.1 [1.3]***</b>		+48.5[11.1]	<b>-10.1 [1.3]***</b>
<b>Autumn (MAM)</b>						
CRE mean	+10.7[34.5]	+6.9[32.4]	<b>-3.8 [3.9]</b>		-5.9[28.9]	<b>-16.6 [3.7]***</b>
CRE <sub>SW</sub> mean	-50.8[34.4]	-48.2[33.0]	<b>+2.6 [3.9]</b>		-48.8[30.5]	<b>+2.0 [3.8]</b>
CRE <sub>LW</sub> mean	+61.5[11.0]	+55.1[10.3]	<b>-6.4 [1.2]***</b>		+42.9[10.2]	<b>-18.6 [1.2]***</b>
<b>Winter (JJA)</b>						
CRE mean	+38.4[14.8]	+33.7[14.6]	<b>-4.7 [1.5]**</b>		+16.5[12.0]	<b>-21.9 [1.4]***</b>
CRE <sub>SW</sub> mean	-24.2[13.5]	-24.7[13.6]	<b>-0.5 [1.4]</b>		-24.1[12.5]	<b>0.1 [1.4]</b>
CRE <sub>LW</sub> mean	+62.6[11.6]	+58.4[11.5]	<b>-4.2 [1.2]***</b>		+40.6[9.7]	<b>-22.0 [1.1]***</b>
<b>Spring (SON)</b>						
CRE mean	-53.9[55.4]	-45.7[44.3]	<b>+8.2 [5.3]</b>		-57.1[45.4]	<b>-3.2 [5.3]</b>
CRE <sub>SW</sub> mean	-115.1[60.0]	-99.3[49.8]	<b>+15.8 [5.8]**</b>		-105.7[51.8]	<b>+9.4 [5.9]</b>
CRE <sub>LW</sub> mean	+61.2[13.3]	+53.6[12.4]	<b>-7.6 [1.3]***</b>		+48.6[12.5]	<b>-12.6 [1.4]***</b>

All values have units of watts per square meter (W m<sup>-2</sup>). The bold values indicate the biases, which were calculated based on mean surface fluxes (e.g., ACCESS-AM2 – observation, CERES – observation). When present, brackets “[]” show the day-to-day standard deviation, while bolded brackets show the standard error of the mean difference. The biases with “\*\*” mean the *p* value < 0.1, biases with “\*\*\*” mean the *p* value < 0.01, and biases with “\*\*\*\*” mean the *p* value < 0.001.

same pattern as the ACCESS-AM2 model (Table 2, Fig. 5b). However, larger negative biases of  $\text{CRE}_{\text{LW}}$  in autumn and winter than the model can be attributed to the large LW bias during these seasons in the satellite measurements (Table 1, Fig. 5c). The overestimation of surface total CRE in ACCESS-AM2 is consistent with a series of studies (Allan, 2000; Protat et al., 2017; McFarquhar et al., 2021), with the source of overestimated surface SW radiation attributed to poor simulation of low-level cloud fraction and cloud liquid water content.

The diurnal cycle of CRE biases in summer was investigated in Appendix B. For ACCESS-AM2, the prevalent  $\text{CRE}_{\text{SW}}$  biases contribute to the majority of the CRE bias, which peaks at noon and presents no bias at night. The  $\text{CRE}_{\text{LW}}$  biases have a lower magnitude than  $\text{CRE}_{\text{SW}}$  and show no obvious variability (Fig. B1). For CERES,  $\text{CRE}_{\text{SW}}$  biases are comparable to ACCESS-AM2, while the negative  $\text{CRE}_{\text{LW}}$  biases are substantial at local night (Fig. B1), which has been attributed to wrong cloud base height (Hinkelmann and Marchand, 2020). The diurnal cycle highlights that in summer the ACCESS-AM2 model is able to more accurately capture the characteristics of LW radiation than it can for SW radiation, and most of the cloud radiative biases can be attributed to poor simulation of SW radiation. While in CERES, poor SW simulation during the day and LW simulation during the night both contribute to the total cloud radiative biases.

#### 4 CF biases and their connection to radiative biases

After finding non-negligible radiative biases in the surface radiation and CRE in the ACCESS-AM2 model and CERES product, we now examine the cloud conditions associated with these biases. In line with theoretical expectation and previous studies that suggest the CF has a significant influence on the downwelling surface radiation (Luo et al., 2016; Protat et al., 2017), we evaluate the distribution of the CF and its relationship with radiative bias using daily observational data collected by cloud camera during MICRE from April 2016 to March 2018.

##### 4.1 CF distribution

The annual (a) and seasonal (b–e) CF distributions are shown in Fig. 6. In the left panel, the daily averaged CFs for the observations and model are, respectively,  $0.81 \pm 0.19$  and  $0.82 \pm 0.17$ . The number following the  $\pm$  sign here indicates the daily standard deviation of the CF. The mean bias (ACCESS-AM2 – observation) is the integrated effect of an underestimated frequency of the CF between 0.2 and 0.6 and an overestimated frequency of the CF between 0.6 and 0.9 (Fig. 6a). As shown in Fig. 6e, the model accurately simulates the mean CF in the spring, but it still overestimates the CF frequency between 0.6 and 0.9. In both autumn and winter, the model overestimated the mean CF, with a more

pronounced overestimation occurring in winter (Fig. 6c, d). Unlike spring, autumn, and winter, the summer mean CF in the model is lower than observed (Fig. 6b).

Several previous studies examined the CF simulated by climate models or reanalysis in the SO and Antarctic regions during austral summer (Mason et al., 2015; Protat et al., 2017; Wang et al., 2020; McFarquhar et al., 2021). In the ACCESS1.3 model for the high-latitude SO ( $50\text{--}65^\circ \text{S}$ ), Mason et al. (2015) found an overall CF deficit. Protat et al. (2017) discovered that the regional NWP version of the ACCESS model overestimates the frequency of intermediate CF but underestimates the frequency of an extremely low or extremely high CF over the SO. Wang et al. (2020) found an underestimation of the daily averaged CF in the ERA5 datasets. In McFarquhar et al. (2021), the radiation bias in the NWP version of ACCESS was shown to link mostly to low-level clouds.

During MICRE, the sky was overcast over almost the entire observation period (bar 4d). As mentioned in the previous section, our study also finds a total overestimation for average downwelling surface SW radiation in the ACCESS-AM2 model. However, here we show mean overestimations in the CF by the model in autumn and winter, a result of both an overestimation in the frequency of the CF between 0.6 and 0.9 and an underestimation of other CFs. In the winter, when the SW bias is negative, there is a positive bias in the CF. In summer we find an underestimation of the CF, when the positive SW bias is particularly evident, which agrees with the previous studies' conclusions. Nevertheless, the overall overestimated CF and positive surface SW biases in the model indicate that the CF alone does not control the cloud radiative effect, but also properties such as cloud phase, cloud base height, and cloud geometrical or optical thickness are likely to play a significant role (Viúdez-Mora et al., 2015; Cesana and Storelvmo, 2017; Fiddes et al., 2022). In addition, cloud microphysics such as ice crystal shape and size distribution and direct and indirect effect of aerosols could also have an effect on radiation biases (Bohren and Huffman, 2008; Kuma et al., 2020). Our results here are in agreement with the work done by Schuddeboom and McDonald (2021), which found an overestimated low-level CF and a reduced reflectivity of low-level cloud over the SO in CMIP6 models, highlighting the significance of correctly representing low-level clouds to simulating radiative balance over the SO. In the next section, we examine how the CF influences the radiation and, as a result, the CRE.

##### 4.2 CF distribution with respect to different radiation biases

Figure 7 shows the CF distribution divided into different radiation bias cases over the entire time series. Figure 7a shows where the SW bias is large and negative, represented by the 10th percentile (smaller than  $-20 \text{ W m}^{-2}$ ). Figure 7b is where the SW bias is small, between the 30th and 70th per-

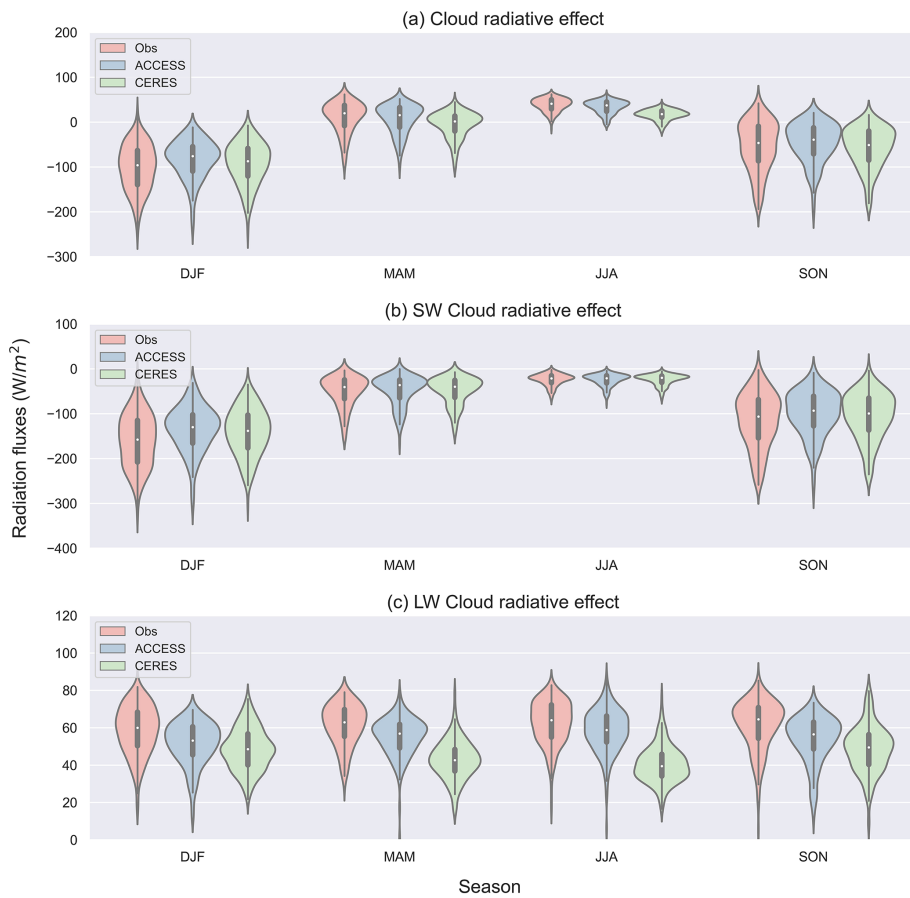


**Figure 5.** Same as Fig. 3 but for CREs among surface observations, the ACCESS-AM2 model, and satellite observations.

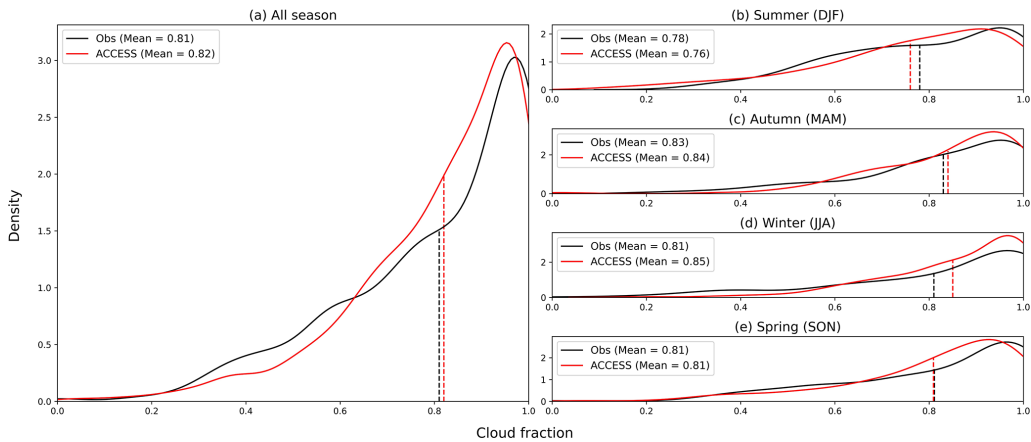


**Figure 6.** The total CF distribution (a) and seasonal CF distribution (b, c, d, e) of ACCESS-AM2 model and surface observations from April 2016 to March 2018. The vertical dashed lines indicate the mean of the datasets corresponding to their color. Averages are shown in the brackets in the legend.

centile (within  $\pm 10 \text{ W m}^{-2}$ ), and Fig. 7c is where the SW difference is large and positive, represented by the 90th percentile (larger than  $50 \text{ W m}^{-2}$ ). For LW cases on the right panels, the selection criterion is identical in terms of per-

centiles to the SW cases, but with different thresholds as indicated.

In Fig. 7a, showing the negative SW bias condition, an evident overestimation of the CF in the model is found, particularly at higher frequencies of CFs above 0.8. For Fig. 7b,

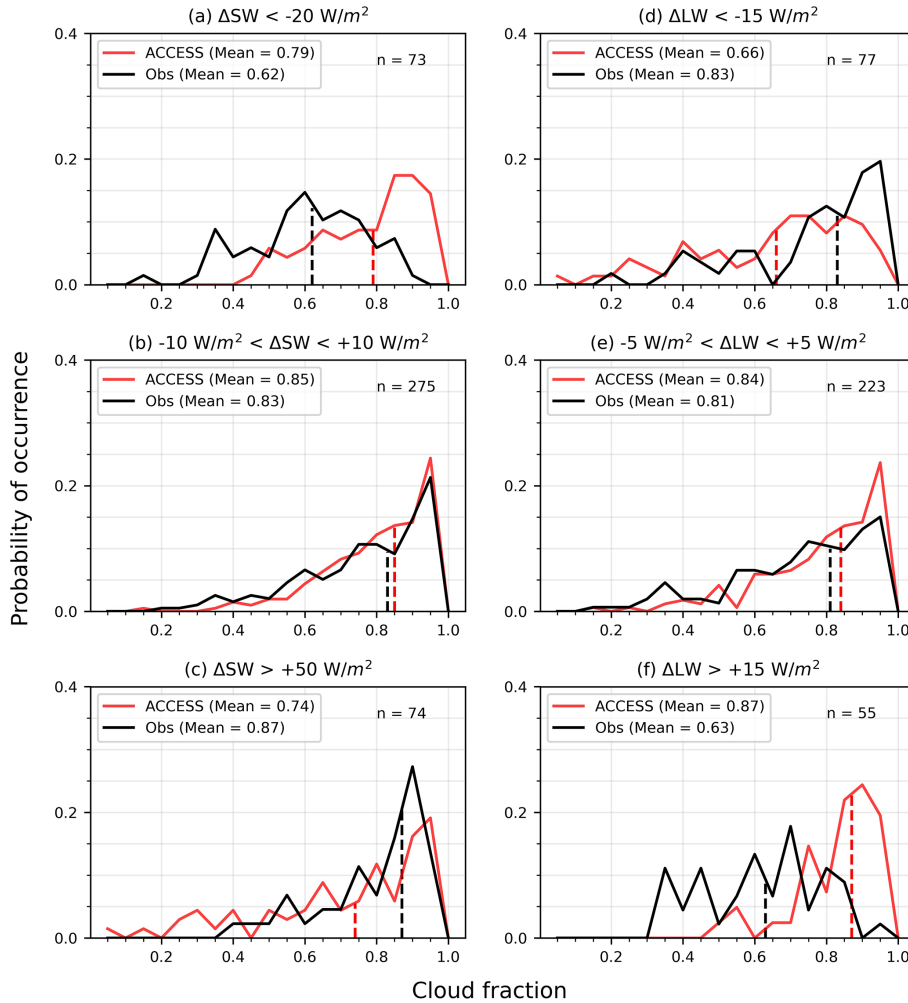


**Figure 7.** Daily averaged CF distributions from the ACCESS-AM2 model (red) and observation (black), restricted to cases where down-welling surface (a)  $\Delta\text{SW}$  (ACCESS-AM2 – observation)  $< -20 \text{ W m}^{-2}$ , (b)  $-10 \text{ W m}^{-2} < \Delta\text{SW} < 10 \text{ W m}^{-2}$ , (c)  $\Delta\text{SW} > 50 \text{ W m}^{-2}$ , (d)  $\Delta\text{LW}$  (ACCESS-AM2 – observation)  $< -15 \text{ W m}^{-2}$ , (e)  $-5 \text{ W m}^{-2} < \Delta\text{LW} < -5 \text{ W m}^{-2}$ , and (f)  $\Delta\text{LW} > 15 \text{ W m}^{-2}$ . The amount of data in each case is annotated on the top right of the panel. The vertical dashed lines indicate the mean of the datasets corresponding to their color. Averages are shown in the brackets in the legend.

the CF in the model conforms well to the observation with a 0.02 difference on average. When the SW bias corresponded to a strong positive value (Fig. 7c), the model largely underestimated the CF by overestimating the frequency of low CF (smaller than 0.4) and underestimating the frequency of high CF (larger than 0.8).

For panels on the right depicting the conditions restricted by the LW bias, Fig. 7d shows that when there was a strong negative LW bias, the CF simulated by the model was significantly lower than the observations, influenced by a large underestimation of the CF frequency of above 0.8. When the LW bias is relatively low (Fig. 7e), the simulated CF was comparable to the observation, with a bias of 0.03 on average. During large and positive LW bias conditions (Fig. 7f), the model overestimated the CF by simulating too much high CF.

The analysis above demonstrates that the radiative biases at the extremes can be associated with biases in the CF, where SW radiation is underestimated with a greater CF and is overestimated with a lower CF. LW radiation appears to consistently respond by following the opposite mechanism. For the majority of the time, however, when radiative biases are small, we find that the model performs surprisingly well with respect to the CF. This result suggests more attention should be paid to instances when the radiative biases are strongly positive or negative to understand what type of cloud conditions are contributing to these biases (e.g., cloud top pressure, cloud optical and geometrical depth). Moreover, it is worth noting that limitations exist in comparing the CF derived from a camera versus a model as they have different spatial coverage. While much of that is smoothed out by taking daily averages, the statistics could still be affected.

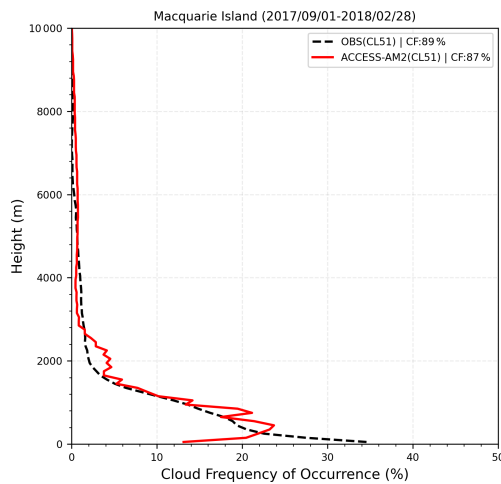


**Figure 8.** CFO histogram against height above the mean sea level observed at Macquarie Island (black) and simulated by the lidar simulator based on atmospheric fields for ACCESS-AM2 model (red), from September 2017 to February 2018. The total CF is shown in the legend. The height of this plot is limited to 10 km as there was no significant amount of cloud detected above this level.

## 5 Cloud frequency of occurrence

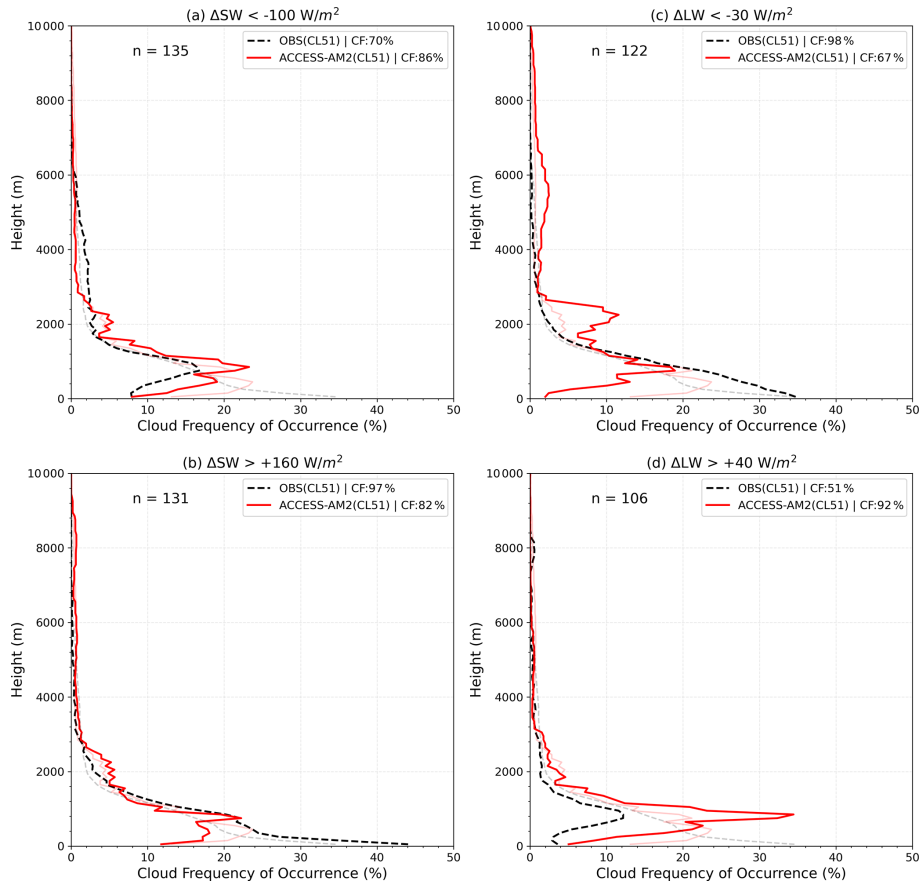
The ALCF product was operated using the hourly data from the ACCESS-AM2 model and ceilometer data from September 2017 to February 2018. Figures 8 and 9 show the likelihood of cloud occurrence with height over this period of time. The CF in the figure caption denotes the overall CF collected by the ceilometer over the 6-month period as calculated by the ALCF, which might include both fog and precipitation. The averaged CFO and CF of 10 subcolumns are chosen to represent the model's statistics. The results in this section can be seasonally biased as the date range is not an integer number of years. The different magnitudes of overestimation or underestimation of the CF compared with previous results in Sect. 4.2 may be attributed to the different time period of the data. Additionally, different viewing geometry (the ceilometer only sees directly overhead, whereas the camera sees a much larger part of the sky), detection thresholds, any errors in cloud detection (incomplete overlap near the surface in the ceilometer), or precipitation misidentified as cloud could cause the differences in the CF measured by the cloud camera and ceilometer.

Figure 8 shows the histogram of CFO, measured by the ceilometer at Macquarie Island, versus height above the mean sea level. It demonstrates an observed predominant low-level cloud between the surface and 2 km height. Cloud occurrence was found 35 % of the time near the lowest level (around 50 m) provided by the ALCF. As the altitude increases, cloud occurrence declines rapidly, reaching close to zero above 6 km, which could be partially due to the backscatter attenuation caused by low-level clouds (McErlich et al., 2021). In comparison, the model has a large un-

derestimation of cloud occurrence at the lowest level where only about 13 % of the cloud occurrence is detected near the surface. It reaches a peak at around 500 m and then gradually diminishes with height. In contrast to the ceilometer, the model detected small cloud occurrences above 6 km. The overall CF for this period (spring and summer) observed by the ceilometer was 89 %, which the model underestimated by 2 %.

Ceilometers determine the CBH from the backscatter profile, and higher clouds can be obscured by optically thick low-level water clouds, rendering high-level clouds invisible in the profile (Klekociuk et al., 2020; Kuma et al., 2021b; McErlich et al., 2021). The limitation of the ceilometer is likely the explanation for why clouds above 6 km are unaccounted for in these observations. A multilayer cloud occurrence of 19.5 % was obtained by Protat et al. (2017) within a span of 10 d between latitudes of 43 and 48° S. Klekociuk et al. (2020) found a 26 % occurrence of multilayer cloud during a 2-month campaign from latitudes 44.7 to 67° S. By examining these previous observations, we can have an approximation of the frequency at which the ceilometer experiences the limitation of high cloud obscurity over the SO. As the ACCESS-AM2 outputs are passed through the ALCF, the same limitation applies to the modeled data. Therefore, we can fairly compare the characteristics of low-level clouds between the ceilometer and model. When using the ALCF to replicate what the model "observes" if it were a ceilometer, Fig. 8 highlights that the ACCESS-AM2 model tends to underestimate the total CF and can only partially reproduce low-level cloud below 300 m while slightly overestimating the cloud occurrence between 300 m and 3 km, with the largest overestimation of 5 % observed at 800 m. In Fiddes et al. (2022) it was found that the ACCESS-AM2 model, when compared to COSP satellite products, underestimates low clouds at the expense of mid-level clouds. The NWP version of the ACCESS model underestimated the low-level cloud occurrence below 1.5 km and largely overestimated the frequency of multilayer cloud, consistent with the excess surface SW radiation in the model (Protat et al., 2017). Different from prior studies that demonstrated an overall underestimation of low-level clouds below 2 km in the ACCESS model, our findings suggested a specific underestimation of low-level clouds below 300 m and an overestimation for other low-level clouds above this altitude. The general underestimation of the total CF conforms to previous studies that used the ALCF to assess the performance of several climate models and reanalysis products (Kuma et al., 2020, 2021b).

Nevertheless, it is crucial to note that limitations exist in the ALCF for reproducing CFO. As mentioned in Sect. 2.6, the ALCF does not identify precipitation, which could be classified as cloud in the ceilometer while ignored in the model (Kuma et al., 2021b). This may cause an overestimation of CFO near the surface in the ceilometer and potentially amplify the underestimation of low-level CFO in the model. Upon visually inspecting the time series of ceilome-



**Figure 9.** Same as Fig. 8 but restricted with different bias conditions, where (a)  $\Delta SW$  (ACCESS-AM2 – observation)  $< -100 \text{ W m}^{-2}$ , (b)  $\Delta SW > 160 \text{ W m}^{-2}$ , (c)  $\Delta LW$  (ACCESS-AM2 – observation)  $< -30 \text{ W m}^{-2}$ , and (d)  $\Delta LW > 40 \text{ W m}^{-2}$ . The lighter shaded lines indicate the total cloud occurrences as in Fig. 8.

ter backscatter profiles, certain layers beneath stratocumulus clouds at around 500 m are identified as clouds, potentially consisting of drizzle, snow, or fog. Tansey et al. (2022) has reported an occurrence of 34 % and 19 % of drizzle in 2016–2017 spring and summer at Macquarie Island. Moreover, Stanford et al. (2023) found that ceilometer observations on Macquarie Island were obscured 18 % of the time because of fog, which is also likely to influence the CFO near the surface. Hence, low-level CFO below 500 m should be interpreted cautiously as it could be influenced by the combination of precipitation and fog. Further research that combines lidar/ceilometer with precipitation measurements will be beneficial to the model evaluation. Moreover, more sophisticated algorithms to classify precipitation, fog, and aerosol are suggested to be developed within the ALCF.

To further explore the relationships of cloud occurrence with the radiative biases, we next evaluate the cloud occurrence under different radiation bias conditions, as described in the previous section. Figure 9 shows the histograms of cloud occurrence and the total CF in different radiation bias conditions, noting that we are not showing the cloud occur-

rence profiles under neutral bias conditions, as the model performed very similarly to the mean shown in Fig. 8 for both SW and LW conditions.

When SW biases are large and negative, as per the 10th percentile, the model generates 16 % higher total CF than the observations and simulates the same cloud occurrence of 8 % near the surface (Fig. 9a). There is a persistent overestimation of cloud occurrence between the surface and 2.5 km in the model, compensated for by the underestimation of cloud occurrence between 2.5 and 6 km. The observed CFO in these conditions is smaller than that observed under average conditions at lower levels, as seen in Fig. 8 and replotted in Fig. 9 in lighter colors. The model, however, sees an increase in CFO above 1 km altitude. When the SW bias is large and positive (Fig. 9b), as per the 90th percentile, the model underestimates the cloud occurrence below 1.5 km but up to 32 % near the surface. The model's low-level cloud occurrence below 1 km decreased from the mean (Fig. 8), while the observed low-level CFO has clearly increased. The total CF simulated by the model was lower than observed by 15 % in these cases.

Figure 9c, in which cases of large negative LW biases were selected by the 10th percentile, demonstrates a strong underestimation by the model of cloud occurrence below 1 km and a significant overestimation between 1.5 and 3 km. The ALCF model output overestimates clouds above 4 km, possibly offset by the scarce simulated low-level clouds. The model output is also clearly different to that of the mean modeled occurrence profile, where low-level cloud below 1 km occurred less frequently. This is in contrast to the observed profile, where we see more frequent cloud occurrences between the surface and approximately 1.5 km. The total modeled CF was lower than the observed values by 31 %. When the LW bias is large and positive (Fig. 9d), as per the 90th percentile, the model tends to overestimate the cloud occurrence below around 3 km and significantly overestimate the total CF by 41 %. The observed low-level CFO is lower than the average conditions in these cases, with a similar profile to that of the underestimated SW bias profile (Fig. 9a). Below 500 m, the modeled cloud occurrence is lower than the average, but greater between this level and 2 km.

Combining the cloud occurrence and CF over different bias conditions above, excessive downwelling surface SW radiation in the model was associated with a lower low-level cloud occurrence and lower CF, which aligns with our expectations. The mid- and high-level clouds can be simulated by the model even though the model underestimates low-level clouds. The minor changes in the modeled cloud occurrence profiles between both SW conditions and the mean demonstrate the model's inability to capture a diverse range of cloud types, as found in Fiddes et al. (2022). However, this relative consistency in vertical cloud profile appears to be less apparent when considering the LW conditions. For the LW bias conditions, larger differences in the modeled low-level cloud occurrence profiles are observed, when compared to the mean. This may suggest that the CFO of low-level clouds has a larger controlling factor over the LW biases than that of the SW biases.

Despite the large influence of cloud macrophysical characteristics such as the CF and CFO on cloud radiative properties, it is essential to acknowledge the crucial role played by cloud microphysical properties such as cloud phase, cloud droplet number concentration, and cloud effective radius. Vergara-Temprado et al. (2018) emphasized the significance of incorporating the spatial and temporal variations of ice-nucleating particle (INP) concentrations in the cloud microphysics scheme. More realistic INP distributions and cloud microphysical properties are crucial to accurately simulate cloud phase, cloud reflectance, and thus radiation (Tan and Storelvmo, 2016; Furtado and Field, 2017). Gettelman et al. (2020) compared cloud microphysics in a nudged global climate model (the Community Atmosphere Model, CAM) with aircraft observations (the Southern Ocean Clouds, Radiation, Aerosol Transport Experimental Study, SOCRATES) collected over the SO. An improved simulation of SW CRE was shown by implementing a revised autoconversion

scheme that reduces both liquid and ice water path but increases cloud fraction and effective radius, maintaining more supercooled liquid water. Nevertheless, the model still fell short of matching the droplet numbers observed in aircraft measurements, which suggests that higher concentrations of cloud condensation nuclei (CCN) and greater droplet numbers may be required to achieve better agreement (Gettelman et al., 2020). In light of these preceding studies, a more detailed understanding of cloud macro- and microphysical properties is necessary to correctly simulate the radiation balance in climate models.

## 6 Conclusions

In this work, we provided an evaluation of the radiation fluxes, CRE, CF, and cloud occurrence for the ACCESS-AM2 model using surface-based observations between April 2016 and March 2018 at Macquarie Island. In addition, we evaluated the radiation fluxes and CRE for the CERES SYN 1° surface-based product over the same period. Moreover, we used the newly developed lidar simulator, the ALCF, to quantify the relationship between cloud occurrence and radiation biases in the model.

For the ACCESS-AM2 model, there was an overestimation of  $+9.5 \pm 33.5 \text{ W m}^{-2}$  for downwelling surface SW radiation fluxes and an underestimation of  $-2.3 \pm 13.5 \text{ W m}^{-2}$  for LW radiation fluxes in all-sky conditions. The SW bias was more pronounced in spring and summer on account of the reduced low-level CF in the model, as well as strong solar radiation during these seasons. The slight LW bias suggests a good performance of the model in simulating LW radiation on average. Compared to ERA5, a small underestimation of  $-2.3 \pm 3.7 \text{ W m}^{-2}$  for SWcs radiation and a significant overestimation of  $+4.5 \pm 5.3 \text{ W m}^{-2}$  for LWcs were found in the model, despite also being nudged to ERA5. The combination of radiation biases in all-sky and clear-sky conditions contributes to an overestimation of  $+4.8 \pm 28.0 \text{ W m}^{-2}$  for total CRE in the model, dominated by the SW CRE bias of  $+11.2 \pm 31.1 \text{ W m}^{-2}$ . The total CRE bias was more pronounced in summer, which can be attributed to the SW CRE bias. In winter, the LW CRE bias contributes most of the total bias. For the CERES product, there was an overestimation of  $+8.0 \pm 18.0 \text{ W m}^{-2}$  for SW radiation fluxes and an underestimation of  $-12.1 \pm 12.2 \text{ W m}^{-2}$  for LW radiation fluxes in all-sky conditions, with the SW bias dominating in summer and LW bias dominating in winter. These results agree with Hinkelman and Marchand (2020), who showed a poor simulation of low-level CBH at night contributing to the LW bias in the satellite measurements. For clear-sky conditions, the SWcs is well captured by CERES, while the biases of LWcs are significant (despite also using ERA5 to inform the radiative model) and very similar to the model. We speculate that temperature and humidity representation play an important role in causing the LWcs bias in CERES and suggest that

further research should be conducted to evaluate clear-sky radiation properties in CERES and ERA5.

The average CF distribution simulated by the model is comparable with the observations with a bias of 0.01. However, this is caused by an underestimated frequency of the CF between 0.2 and 0.6 and an overestimated frequency of the CF above 0.6. Unlike prior summer-focused studies that found an underestimation of the CF in the model, in this study we found an overestimation of the mean CF across the year (0.01) with the exception of a slight underestimation in summer (0.02). This highlights the need for greater model evaluation throughout the seasons as the summer biases may not be representative throughout the year. When restricting the CF to different radiation bias conditions, an overestimation of surface SW radiation was associated with an underestimation of the CF, and an underestimation of surface SW radiation was associated with an overestimation of the CF. The opposite was found for LW cases.

By using the ALCF we can compare ceilometer data with the model data directly. Overall, the results highlighted an underestimation of low-level cloud occurrence below 300 m and the total CF, which may be biased due to the presence of precipitation and fog. When evaluating cloud occurrence under different radiation bias conditions, it was demonstrated that an overestimation of SW radiation is associated with an underestimation of the low-level cloud occurrence and CF, and negative SW radiation biases were associated with an overestimated low-level cloud occurrence. For different LW bias conditions, the results are opposite to the SW bias conditions, as expected. An overestimation of LW radiation is associated with an overestimation of low-level cloud occurrence below 3 km, while the model severely underestimates low-level cloud occurrence for negative LW bias conditions. We suggest that the larger differences in the modeled low-level cloud occurrences between the LW conditions demonstrate the greater dependence on low-level CFO of the LW biases than SW biases.

Aside from the erroneous cloud representation in the model, radiative biases could also arise from data collection and processing, which must be considered. For example, observed missing data on specific days have been ignored. The simulated clear-sky radiations are based on the modeled ERA5 product, which will include inaccuracies on clear-sky radiation estimation due to inaccurate temperature and humidity profiles. The calculation of the all-sky CF is influenced by the presence of sun in the cloud images. This results in a saturation of a portion of the fisheye image, resulting in uncertainty in the estimated CF. Additionally, the limitation of the ceilometer (in both the observations and the ALCF-derived product) in detecting high-level clouds adds difficulty for complete model comparison. For the ACCESS-AM2 and CERES, the Macquarie Island location is interpolated from coarse-resolution grid boxes, which will also bring about some unavoidable biases.

Overall, this study reinforces the finding of excess downwelling surface SW radiation in the ACCESS-AM2 model. The significant bias of surface radiation fluxes in the SO in CERES, which can lead to an underestimation of model bias, indicates the requirement to also continually evaluate satellite products using ground-based observations. We also highlight the need to investigate what an accurate representation of clear sky is in the SO, given the difficulty in validating current clear-sky models due to consistent cloudiness and its necessity in calculating the CRE. Moreover, this work confirms that the CF and cloud occurrence have a large impact on the surface radiation, though with differing importance for the SW and LW biases. We suggest that this demonstrates the lack of diversity of clouds represented by the model, as suggested by Fiddes et al. (2022), and also that other cloud microphysical properties, such as cloud phase, cloud effective radius, and cloud droplet size distribution, may be more important than the vertical profile for the SW biases. We emphasize that the correct representation of supercooled liquid water over the SO is important for modeling the radiation in the region, as inadequate supercooled liquid water content will cause less reflectivity of clouds and result in positive downwelling surface SW biases (Luo et al., 2016; Vergara-Temprado et al., 2018; Gettelman et al., 2020).

For future studies, further evaluation of the climate models at more locations over the SO is suggested to comprehensively investigate the radiation biases over this region. In the latest Guyot et al. (2022) study, the ALCF can now be used to detect the cloud phase, enabling future studies to address the role that cloud phase plays in influencing the radiation biases by further utilizing this tool. In addition, satellite products which showed non-negligible biases require further evaluation and development in surface radiation retrievals since this is still the primary tool in use for evaluating the model.

## Appendix A: Validation of the measurements of AAD's radiometers against the colocated ARM radiometers

Here we compare radiation measurements derived from radiometers deployed by AAD against co-located radiometers deployed by ARM (McFarquhar et al., 2021) to validate both datasets. Seasonal comparisons were made for SW radiation (Fig. A1, left) from 4 April 2016 to 6 March 2018 and LW radiation (Fig. A1, right) from 15 August 2016 to 6 March 2018. The linear regression coefficients range from 0.94 to 1.01 with no obvious seasonal differences, which depicts a good consistency between two datasets. Additionally, hourly comparisons were also plotted for two datasets with their 95 % confidence intervals (Fig. A2). Both datasets appear to agree and are for the majority of the time within the 95 % confidence intervals. This analysis suggests there is little meaningful difference between the two co-located instruments, giving us confidence in our results.

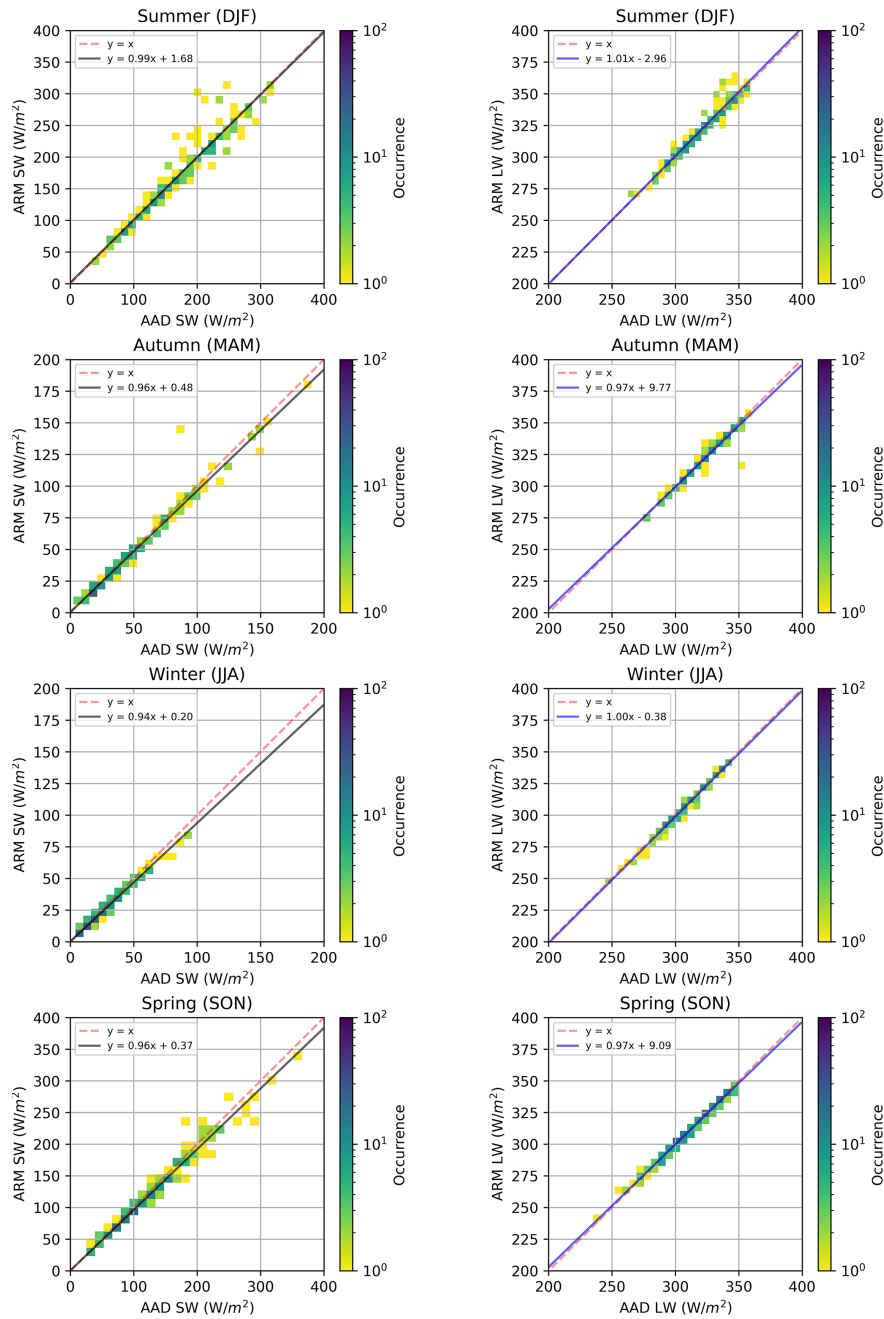


**Figure A1.** The seasonal comparisons of radiometers between AAD and ARM for 4 April 2016 to 6 March 2018 (pyranometer) and for 15 August 2016 to 6 March 2018 (pyrgeometer). Radiation data are averaged daily, and linear fit parameters are detailed.

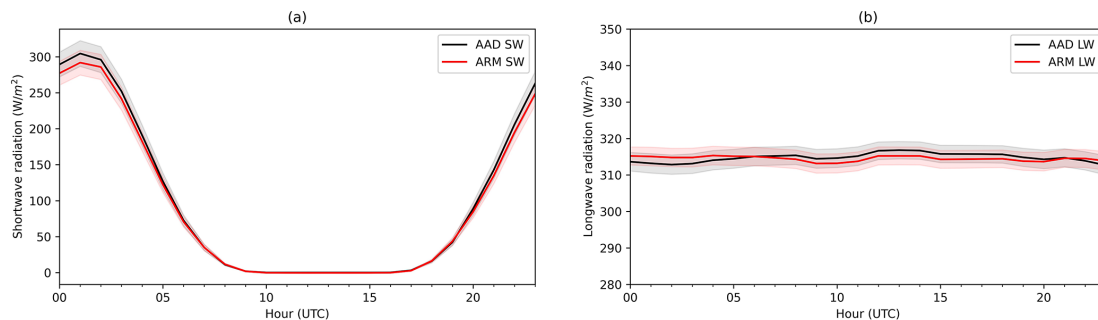


**Figure A2.** Hourly plots of SW (a) and LW (b) radiation data for AAD and ARM measurements, with the shaded areas showing the 95 % confidence intervals.

## Appendix B: Diurnal cycle and bias of total CRE, $\text{CRE}_{\text{SW}}$ , and $\text{CRE}_{\text{LW}}$

In this section the CRE biases over the diurnal cycle were explored. We now consider only the period of September 2017 to February 2018 where hourly instantaneous output was available from the ACCESS-AM2 model. Figure B1 shows the diurnal cycle of total CRE,  $\text{CRE}_{\text{SW}}$ , and  $\text{CRE}_{\text{LW}}$  (top) and the associated biases compared with ground-based observations (bottom).

For ACCESS-AM2 total CRE (Fig. B1a, d), small negative biases are found during the nighttime due to the lack of incoming solar radiation, contributed by the biases in  $\text{CRE}_{\text{LW}}$ . The highest difference for total CRE occurs around 01:00 UTC (approximately local solar noon), when the difference is roughly  $+57 \text{ W m}^{-2}$ .  $\text{CRE}_{\text{SW}}$  has a similar diurnal cycle to the total CRE's, with the bias peaking at the same time as total CRE's. Throughout the day, the  $\text{CRE}_{\text{LW}}$  is comparable with surface observations and shows no diurnal variability (see y-axis scale in Fig. B1c). The CERES  $\text{CRE}_{\text{SW}}$  bias exhibits similarities to ACCESS-AM2, while it is larger during specific periods, such as 04:00 UTC and 19:00–21:00 UTC (Fig. B1e). Different to ACCESS-AM2, the CERES  $\text{CRE}_{\text{LW}}$  has notable negative biases at night local time (07:00–18:00 UTC), with biases ranging from  $-20$  to  $-15 \text{ W m}^{-2}$ . The significant underestimation of  $\text{CRE}_{\text{LW}}$  in CERES, as highlighted in Hinkelmann and Marchand (2020), is attributed to incorrect cloud base height during local nighttime periods (Fig. B1c, f).

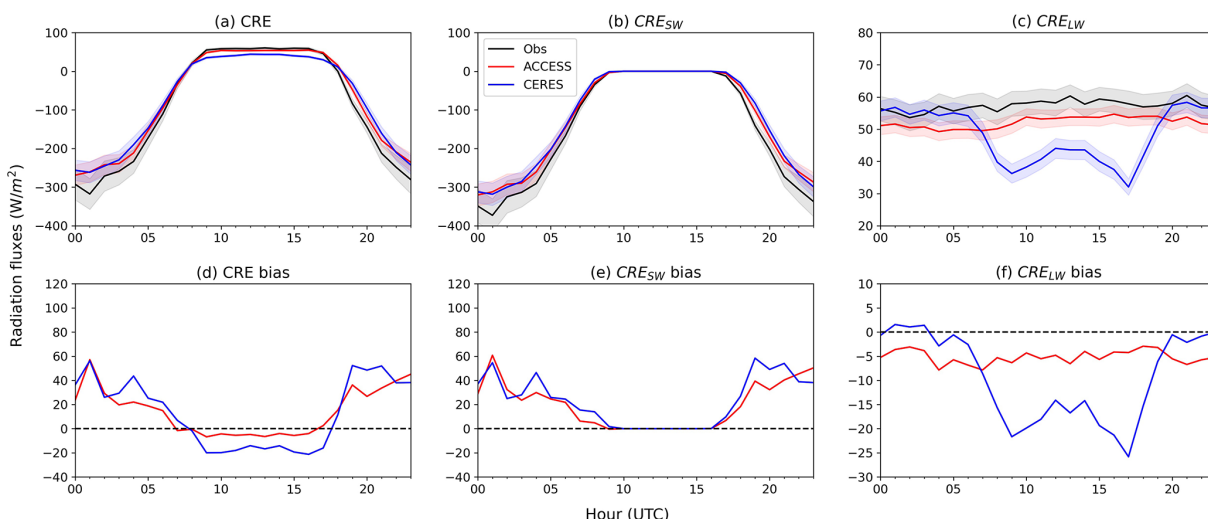


**Figure B1.** Diurnal cycle of the ACCESS-AM2, CERES, and observational CRE (a),  $\text{CRE}_{\text{SW}}$  (b), and  $\text{CRE}_{\text{LW}}$  (c) in the top row associated with the biases (ACCESS-AM2 – observation; CERES – observation) in the bottom row (d, e, f), based on data from September 2017 to February 2018. The shaded areas of the panels above represent the 95 % confidence interval of the value.

**Data availability.** The ARM radiometer data collected during MICRE are available via the ARM data archive at <https://doi.org/10.5439/1377836> (Sengupta et al., 2016). The AAD radiometer and all-sky cloud camera data are available from the Australian Antarctic Data Centre (AADC) at <https://doi.org/10.26179/6seh-er53> (French et al., 2023). The University of Canterbury's Vaisala CL51 ceilometer data are available at AADC (<https://doi.org/10.26179/5d91835e2ccc3>, Alexander and McDonald, 2020). The code for this paper and source of ACCESS-AM2 data is available at <https://doi.org/10.5281/zenodo.10082306> (Pei and Fiddes, 2023). The satellite data (CERES SYN1deg) are available via the CERES data products at <https://ceres.larc.nasa.gov/data/> (NASA, 2023). The ERA5 data are available via the Copernicus data portal at <https://doi.org/10.24381/cds.adbb2d47> (Hersbach et al., 2023). The ALCF is open source and available at <https://github.com/alcf-lidar/alcf> (last access: 21 January 2023) and on Zenodo at <https://doi.org/10.5281/zenodo.4411633> (Kuma et al., 2021a).

**Author contributions.** ZP completed the data processing, analysis, and manuscript writing. SF provided the model simulations. JF provided data processing for raw observational data. PK contributed to the operation of the ALCF. SA and AM provided the observational data at Macquarie Island. ZP, SF, SA, JF, and MM contributed to the project planning and data processing. All authors contributed to the revisions of this paper.

**Competing interests.** The contact author has declared that none of the authors has any competing interests.

**Disclaimer.** Publisher's note: Copernicus Publications remains neutral with regard to jurisdictional claims made in the text, published maps, institutional affiliations, or any other geographical representation in this paper. While Copernicus Publications makes every effort to include appropriate place names, the final responsibility lies with the authors.

**Acknowledgements.** This project received grant funding from the Australian Government as part of the Antarctic Science Collaboration Initiative program, under the Australian Antarctic Program Partnership, ASCI000002. This research was undertaken with the assistance of resources and services from the National Computational Infrastructure (projects jk72, hh5, and rt52), which is supported by the Australian Government. Technical and logistical support for the deployment to Macquarie Island were provided by the Australian Antarctic Division through Australian Antarctic Science Project 4292, and we thank Andrew Klekociuk, Peter de Vries, Terry Egan, Nick Cartwright and Ken Barrett for all of their assistance. ZP and SF would like to thank the ARC Centre of Excellence for Climate Extremes computer modeling support team for their maintenance of virtual environments and code/model support. PK would like to thank the nextGEMS project funded by the European Union Horizon 2020 grant number 101003470. The authors would like to acknowledge the teams at the DOE ARM, NASA CERES, and ECMWF for making the data used in this work available.

**Financial support.** This research has been supported by the Australian Government (Antarctic Science Collaboration Initiative program, ASCI000002; Australian Antarctic Science Project 4292).

**Review statement.** This paper was edited by Matthew Lebsack and reviewed by Emily Tansey and McKenna Stanford.

## References

- Alexander, S. and McDonald, A.: University of Canterbury's Vaisala CL51 Ceilometer at Macquarie Island 2016–2018, Version 1, Australian Antarctic Data Centre [data set], <https://doi.org/10.26179/5d91835e2ccc3>, 2020.
- Allan, R. P.: Evaluation of simulated clear-sky longwave radiation using ground-based observations, *J. Climate*, 13, 1951–1964, [https://doi.org/10.1175/1520-0442\(2000\)013<1951:EOSCL>2.0.CO;2](https://doi.org/10.1175/1520-0442(2000)013<1951:EOSCL>2.0.CO;2), 2000.
- Bennartz, R., Shupe, M. D., Turner, D. D., Walden, V. P., Steffen, K., Cox, C. J., Kulie, M. S., Miller, N. B., and Pettersen, C.: July 2012 Greenland melt extent enhanced by low-level liquid clouds, *Nature*, 496, 83–86, <https://doi.org/10.1038/nature12002>, 2013.
- Bi, D., Dix, M., Marsland, S., O'farrell, S., Sullivan, A., Bodman, R., Law, R., Harman, I., Srbinovsky, J., Rashid, H. A., Dobrohotoff, P., Mackallah, C., Yan, H., Hirst, A., Savita, A., Dias, F. B., Woodhouse, M., Fiedler, R., and Heerdegen, A.: Configuration and spin-up of ACCESS-CM2, the new generation Australian Community Climate and Earth System Simulator Coupled Model, *Journal of Southern Hemisphere Earth Systems Science*, 70, 225–251, <https://doi.org/10.1071/ES19040>, 2020.
- Bodas-Salcedo, A., Webb, M. J., Bony, S., Chepfer, H., Dufresne, J. L., Klein, S. A., Zhang, Y., Marchand, R., Haynes, J. M., PinCUS, R., and John, V. O.: COSP: Satellite simulation software for model assessment, *B. Am. Meteorol. Soc.*, 92, 1023–1043, <https://doi.org/10.1175/2011BAMS2856.1>, 2011.
- Bodas-Salcedo, A., Williams, K. D., Field, P. R., and Lock, A. P.: The surface downwelling solar radiation surplus over the southern ocean in the met office model: The role of midlatitude cyclone clouds, *J. Climate*, 25, 7467–7486, <https://doi.org/10.1175/JCLI-D-11-00702.1>, 2012.
- Bodas-Salcedo, A., Williams, K. D., Ringer, M. A., Beau, I., Cole, J. N., Dufresne, J. L., Koshiro, T., Stevens, B., Wang, Z., and Yokohata, T.: Origins of the solar radiation biases over the Southern Ocean in CMIP2 models, *J. Climate*, 27, 41–56, <https://doi.org/10.1175/JCLI-D-13-00169.1>, 2014.
- Bodas-Salcedo, A., Hill, P. G., Furtado, K., Williams, K. D., Field, P. R., Manners, J. C., Hyder, P., and Kato, S.: Large contribution of supercooled liquid clouds to the solar radiation budget of the Southern Ocean, *J. Climate*, 29, 4213–4228, <https://doi.org/10.1175/JCLI-D-15-0564.1>, 2016.
- Bodman, R. W., Karoly, D. J., Dix, M. R., Harman, I. N., Srbinovsky, J., Dobrohotoff, P. B., and Mackallah, C.: Evaluation of CMIP6 AMIP climate simulations with the ACCESS-AM2 model, *Journal of Southern Hemisphere Earth Systems Science*, 70, 166–179, <https://doi.org/10.1071/ES19033>, 2020.
- Bohren, C. F. and Huffman, D. R.: Absorption and scattering of light by small particles, John Wiley & Sons, <https://doi.org/10.1002/9783527618156>, 2008.

- Campbell, J. R., Hlavka, D. L., Welton, E. J., Flynn, C. J., Turner, D. D., Spinhirne, J. D., Scott III, V. S., and Hwang, I.: Full-time, eye-safe cloud and aerosol lidar observation at atmospheric radiation measurement program sites: Instruments and data processing, *J. Atmos. Ocean. Tech.*, 19, 431–442, 2002.
- Ceppi, P., Hwang, Y. T., Frierson, D. M., and Hartmann, D. L.: Southern Hemisphere jet latitude biases in CMIP5 models linked to shortwave cloud forcing, *Geophys. Res. Lett.*, 39, 1–5, <https://doi.org/10.1029/2012GL053115>, 2012.
- Cesana, G. and Storelvmo, T.: Improving climate projections by understanding how cloud phase affects radiation, *J. Geophys. Res.-Atmos.*, 122, 4594–4599, 2017.
- Cesana, G. V., Khadir, T., Chepfer, H., and Chiriaco, M.: Southern ocean solar reflection biases in CMIP6 models linked to cloud phase and vertical structure representations, *Geophys. Res. Lett.*, 49, e2022GL099777, <https://doi.org/10.1029/2022GL099777>, 2022.
- Chepfer, H., Bony, S., Winker, D., Chiriaco, M., Dufresne, J.-L., and Sèze, G.: Use of CALIPSO lidar observations to evaluate the cloudiness simulated by a climate model, *Geophys. Res. Lett.*, 35, L15704, <https://doi.org/10.1029/2008GL034207>, 2008.
- Corripio, J. G.: Vectorial algebra algorithms for calculating terrain parameters from dems and solar radiation modelling in mountainous terrain, *Int. J. Geogr. Inf. Sci.*, 17, 1–23, <https://doi.org/10.1080/713811744>, 2003.
- Dommgenget, D. and Flöter, J.: Conceptual understanding of climate change with a globally resolved energy balance model, *Clim. Dynam.*, 37, 2143–2165, 2011.
- Edwards, J. M. and Slingo, A.: Studies with a flexible new radiation code. I: Choosing a configuration for a large-scale model, *Q. J. Roy. Meteor. Soc.*, 122, 689–719, <https://doi.org/10.1256/smsqj.53106>, 1996.
- Eyring, V., Bony, S., Meehl, G. A., Senior, C. A., Stevens, B., Stouffer, R. J., and Taylor, K. E.: Overview of the Coupled Model Intercomparison Project Phase 6 (CMIP6) experimental design and organization, *Geosci. Model Dev.*, 9, 1937–1958, <https://doi.org/10.5194/gmd-9-1937-2016>, 2016.
- Fairall, C., Uttal, T., Hazen, D., Hare, J., Cronin, M. F., Bond, N., and Veron, D. E.: Observations of cloud, radiation, and surface forcing in the equatorial eastern Pacific, *J. Climate*, 21, 655–673, 2008.
- Fiddes, S. L., Woodhouse, M. T., Nicholls, Z., Lane, T. P., and Schofield, R.: Cloud, precipitation and radiation responses to large perturbations in global dimethyl sulfide, *Atmos. Chem. Phys.*, 18, 10177–10198, <https://doi.org/10.5194/acp-18-10177-2018>, 2018.
- Fiddes, S. L., Protat, A., Mallet, M. D., Alexander, S. P., and Woodhouse, M. T.: Southern Ocean cloud and shortwave radiation biases in a nudged climate model simulation: does the model ever get it right?, *Atmos. Chem. Phys.*, 22, 14603–14630, <https://doi.org/10.5194/acp-22-14603-2022>, 2022.
- Field, P. R., Bodas-Salcedo, A., and Brooks, M. E.: Using model analysis and satellite data to assess cloud and precipitation in midlatitude cyclones, *Q. J. Roy. Meteor. Soc.*, 137, 1501–1515, <https://doi.org/10.1002/qj.858>, 2011.
- Franklin, C. N., Sun, Z., Bi, D., Dix, M., Yan, H., and Bodas-Salcedo, A.: Evaluation of clouds in access using the satellite simulator package cosp: Global, seasonal, and regional cloud properties, *J. Geophys. Res.-Atmos.*, 118, 732–748, <https://doi.org/10.1029/2012JD018469>, 2013.
- French, J., Pei, Z., Alexander, S., Fiddes, S., Mallet, M., Kuma, P., and McDonald, A.: Macquarie\_Island\_Radiometer\_and\_AllSkyCam\_Data\_2016-2018, Ver. 1, Australian Antarctic Data Centre [data set], <https://doi.org/10.26179/6seh-er53>, 2023.
- Furtado, K. and Field, P.: The role of ice microphysics parametrizations in determining the prevalence of supercooled liquid water in high-resolution simulations of a Southern Ocean midlatitude cyclone, *J. Atmos. Sci.*, 74, 2001–2021, 2017.
- Gettelman, A., Bardeen, C. G., McCluskey, C. S., Järvinen, E., Stith, J., Bretherton, C., McFarquhar, G., Twohy, C., D'Alessandro, J., and Wu, W.: Simulating Observations of Southern Ocean Clouds and Implications for Climate, *J. Geophys. Res.-Atmos.*, 125, 1–22, <https://doi.org/10.1029/2020JD032619>, 2020.
- Ghonima, M. S., Urquhart, B., Chow, C. W., Shields, J. E., Cazorla, A., and Kleissl, J.: A method for cloud detection and opacity classification based on ground based sky imagery, *Atmos. Meas. Tech.*, 5, 2881–2892, <https://doi.org/10.5194/amt-5-2881-2012>, 2012.
- Guyot, A., Protat, A., Alexander, S. P., Klekociuk, A. R., Kuma, P., and McDonald, A.: Detection of supercooled liquid water clouds with ceilometers: Development and evaluation of deterministic and data-driven retrievals, *Atmos. Meas. Tech. Discuss. [preprint]*, <https://doi.org/10.5194/amt-2022-10>, in review, 2022.
- Hersbach, H., Bell, B., Berrisford, P., Hirahara, S., Horányi, A., Muñoz-Sabater, J., Nicolas, J., Peubey, C., Radu, R., Schepers, D., Simmons, A., Soci, C., Abdalla, S., Abellán, X., Balsamo, G., Bechtold, P., Biavati, G., Bidlot, J., Bonavita, M., De Chiara, G., Dahlgren, P., Dee, D., Diamantakis, M., Dragani, R., Flemming, J., Forbes, R., Fuentes, M., Geer, A., Haimberger, L., Healy, S., Hogan, R. J., Hölm, E., Janisková, M., Keeley, S., Laloyaux, P., Lopez, P., Lupu, C., Radnoti, G., de Rosnay, P., Rozum, I., Vamborg, F., Villaume, S., and Thépaut, J. N.: The ERA5 global reanalysis, *Q. J. Roy. Meteor. Soc.*, 146, 1999–2049, <https://doi.org/10.1002/qj.3803>, 2020.
- Hersbach, H., Bell, B., Berrisford, P., Biavati, G., Horányi, A., Muñoz Sabater, J., Nicolas, J., Peubey, C., Radu, R., Rozum, I., Schepers, D., Simmons, A., Soci, C., Dee, D., and Thépaut, J.-N.: ERA5 hourly data on single levels from 1940 to present, Copernicus Climate Change Service (C3S) Climate Data Store (CDS) [data set], <https://doi.org/10.24381/cds.adbb2d47>, 2023.
- Hinkelmann, L. M. and Marchand, R.: Evaluation of CERES and CloudSat Surface Radiative Fluxes Over Macquarie Island, the Southern Ocean, *Earth and Space Science*, 7, 1–17, <https://doi.org/10.1029/2020EA001224>, 2020.
- Hu, Y., Rodier, S., Xu, K. M., Sun, W., Huang, J., Lin, B., Zhai, P., and Josset, D.: Occurrence, liquid water content, and fraction of supercooled water clouds from combined CALIOP-IR/MODIS measurements, *J. Geophys. Res.-Atmos.*, 115, 1–13, <https://doi.org/10.1029/2009JD012384>, 2010.
- Hurrell, J. W., Hack, J. J., Shea, D., Caron, J. M., and Rosinski, J.: A new sea surface temperature and sea ice boundary dataset for the community atmosphere model, *J. Climate*, 21, 5145–5153, <https://doi.org/10.1175/2008JCLI2292.1>, 2008.
- Hwang, Y. T. and Frierson, D. M.: Link between the double-interropical convergence zone problem and cloud biases over

- the southern ocean, *P. Natl. Acad. Sci. USA*, 110, 4935–4940, <https://doi.org/10.1073/pnas.1213302110>, 2013.
- Hyder, P., Edwards, J. M., Allan, R. P., Hewitt, H. T., Bracegirdle, T. J., Gregory, J. M., Wood, R. A., Meijers, A. J., Mulcahy, J., Field, P., Furtado, K., Bodas-Salcedo, A., Williams, K. D., Copsey, D., Josey, S. A., Liu, C., Roberts, C. D., Sanchez, C., Ridley, J., Thorpe, L., Hardiman, S. C., Mayer, M., Berry, D. I., and Belcher, S. E.: Critical Southern Ocean climate model biases traced to atmospheric model cloud errors, *Nat. Commun.*, 9, 3625, <https://doi.org/10.1038/s41467-018-05634-2>, 2018.
- Idso, S. B.: A set of equations for full spectrum and 8- to 14- $\mu\text{m}$  and 10.5- to 12.5- $\mu\text{m}$  thermal radiation from cloudless skies, *Water Resour. Res.*, 17, 295–304, 1981.
- Illingworth, A., Hogan, R., O'connor, E., Bouniol, D., Brooks, M., Delanoë, J., Donovan, D., Eastment, J., Gassiat, N., Goddard, J., Haefelin, M., Baltink, H. K., Krasnov, O. A., Pelon, J., Piriou, J.-M., Protat, A., Russchenberg, H. W. J., Seifert, A., Tompkins, A. M., van Zadelhoff, G.-J., Vinit, F., Willén, U., Wilson, D. R., and Wrench, C. L.: Cloudnet: Continuous evaluation of cloud profiles in seven operational models using ground-based observations, *B. Am. Meteorol. Soc.*, 88, 883–898, 2007.
- Illingworth, A. J., Cimini, D., Haefele, A., Haefelin, M., Hervo, M., Kotthaus, S., Löhnert, U., Martinet, P., Mattis, I., O'Connor, E. J., and Potthast, R.: How can existing ground-based profiling instruments improve European weather forecasts?, *B. Am. Meteorol. Soc.*, 100, 605–619, 2019.
- Kay, J. E., Wall, C., Yettella, V., Medeiros, B., Hannay, C., Caldwell, P., and Bitz, C.: No access global climate impacts of fixing the Southern Ocean shortwave radiation bias in the Community Earth System Model (CESM), *J. Climate*, 29, 4617–4636, <https://doi.org/10.1175/JCLI-D-15-0358.1>, 2016.
- Klekociuk, A. R., French, W. J. R., Alexander, S. P., Kuma, P., and McDonald, A. J.: The state of the atmosphere in the 2016 southern Kerguelen Axis campaign region, *Deep-Sea Res. Pt. II*, 174, 104550, <https://doi.org/10.1016/j.dsr2.2019.02.001>, 2020.
- Kotthaus, S., O'Connor, E., Münkel, C., Charlton-Perez, C., Haefelin, M., Gabey, A. M., and Grimmond, C. S. B.: Recommendations for processing atmospheric attenuated backscatter profiles from Vaisala CL31 ceilometers, *Atmos. Meas. Tech.*, 9, 3769–3791, <https://doi.org/10.5194/amt-9-3769-2016>, 2016.
- Kremser, S., Harvey, M., Kuma, P., Hartery, S., Saint-Macary, A., McGregor, J., Schuddeboom, A., von Hobe, M., Lennartz, S. T., Geddes, A., Querel, R., McDonald, A., Peltola, M., Sellegri, K., Silber, I., Law, C. S., Flynn, C. J., Marriner, A., Hill, T. C. J., DeMott, P. J., Hume, C. C., Plank, G., Graham, G., and Parsons, S.: Southern Ocean cloud and aerosol data: a compilation of measurements from the 2018 Southern Ocean Ross Sea Marine Ecosystems and Environment voyage, *Earth Syst. Sci. Data*, 13, 3115–3153, <https://doi.org/10.5194/essd-13-3115-2021>, 2021.
- Kuma, P., McDonald, A. J., Morgenstern, O., Alexander, S. P., Cassano, J. J., Garrett, S., Halla, J., Hartery, S., Harvey, M. J., Parsons, S., Plank, G., Varma, V., and Williams, J.: Evaluation of Southern Ocean cloud in the HadGEM3 general circulation model and MERRA-2 reanalysis using ship-based observations, *Atmos. Chem. Phys.*, 20, 6607–6630, <https://doi.org/10.5194/acp-20-6607-2020>, 2020.
- Kuma, P., McDonald, A. J., Morgenstern, O., Querel, R., Silber, I., and Flynn, C. J.: Automatic Lidar and Ceilometer Framework (ALCF), Version 1.0.0, Zenodo [software], <https://doi.org/10.5281/zenodo.4411633>, 2021a.
- Kuma, P., McDonald, A. J., Morgenstern, O., Querel, R., Silber, I., and Flynn, C. J.: Ground-based lidar processing and simulator framework for comparing models and observations (ALCF 1.0), *Geosci. Model Dev.*, 14, 43–72, <https://doi.org/10.5194/gmd-14-43-2021>, 2021b.
- Kuma, P., Bender, F. A.-M., and Jönsson, A. R.: Climate model code genealogy and its relation to climate feedbacks and sensitivity, *J. Adv. Model. Earth Sy.*, 15, e2022MS003588, <https://doi.org/10.1029/2022MS003588>, 2023.
- Lawson, R. P. and Gettelman, A.: Impact of Antarctic mixed-phase clouds on climate, *P. Natl. Acad. Sci. USA*, 111, 18156–18161, <https://doi.org/10.1073/pnas.1418197111>, 2014.
- Li, Q., Lu, W., and Yang, J.: A hybrid thresholding algorithm for cloud detection on ground-based color images, *J. Atmos. Ocean. Tech.*, 28, 1286–1296, <https://doi.org/10.1175/JTECH-D-11-00009.1>, 2011.
- Luo, S., Sun, Z., Zheng, X., Rikus, L., and Franklin, C.: Evaluation of ACCESS model cloud properties over the Southern Ocean area using multiple-satellite products, *Q. J. Roy. Meteor. Soc.*, 142, 160–171, <https://doi.org/10.1002/qj.2641>, 2016.
- Mallet, M. D., Alexander, S. P., Protat, A., and Fiddes, S. L.: Reducing Southern Ocean shortwave radiation errors in the ERA5 reanalysis with machine learning and 25 years of surface observations, *Artificial Intelligence for the Earth Systems*, 2, e220044, <https://doi.org/10.1175/AIES-D-22-0044.1>, 2023.
- Mason, S., Fletcher, J. K., Haynes, J. M., Franklin, C., Protat, A., and Jakob, C.: A hybrid cloud regime methodology used to evaluate Southern Ocean cloud and shortwave radiation errors in ACCESS, *J. Climate*, 28, 6001–6018, <https://doi.org/10.1175/JCLI-D-14-00846.1>, 2015.
- McCoy, D. T., Hartmann, D. L., Zelinka, M. D., Ceppi, P., and Grosvenor, D. P.: Mixed-phase cloud physics and Southern Ocean cloud feedback in climate models, *J. Geophys. Res.-Atmos.*, 120, 9539–9554, 2015.
- McErlich, C., McDonald, A., Schuddeboom, A., and Silber, I.: Comparing Satellite-and Ground-Based Observations of Cloud Occurrence Over High Southern Latitudes, *J. Geophys. Res.-Atmos.*, 126, e2020JD033607, <https://doi.org/10.1029/2020JD033607>, 2021.
- McFarquhar, G. M., Bretherton, C. S., Marchand, R., et al.: Observations of clouds, aerosols, precipitation, and surface radiation over the southern ocean, *B. Am. Meteorol. Soc.*, 102, E894–E928, <https://doi.org/10.1175/BAMS-D-20-0132.1>, 2021.
- Nam, C., Bony, S., Dufresne, J.-L., and Chepfer, H.: The ‘too few, too bright’ tropical low-cloud problem in CMIP5 models, *Geophys. Res. Lett.*, 39, L21801, <https://doi.org/10.1029/2012GL053421>, 2012.
- NASA: CERES Data Products, NASA [data set], <https://ceres.larc.nasa.gov/data/>, last access: 21 January 2023.
- O'Connor, E. J., Illingworth, A. J., and Hogan, R. J.: A technique for autocalibration of cloud lidar, *J. Atmos. Ocean. Tech.*, 21, 777–786, [https://doi.org/10.1175/1520-0426\(2004\)021<0777:ATFAOC>2.0.CO;2](https://doi.org/10.1175/1520-0426(2004)021<0777:ATFAOC>2.0.CO;2), 2004.
- Pei, Z. and Fiddes, S. L.: ACCESS-AM2 daily and hourly cloud and radiation data for model evaluation at Macquarie Island, Zenodo [data set], <https://doi.org/10.5281/zenodo.10082306>, 2023.

- Protat, A., Schulz, E., Rikus, L., Sun, Z., Xiao, Y., and Keywood, M.: Shipborne observations of the radiative effect of Southern Ocean clouds, *J. Geophys. Res.*, 122, 318–328, <https://doi.org/10.1002/2016JD026061>, 2017.
- Ruiz-Arias, J. A., Dudhia, J., Santos-Alamillos, F. J., and Pozo-Vázquez, D.: Surface clear-sky shortwave radiative closure intercomparisons in the Weather Research and Forecasting model, *J. Geophys. Res.-Atmos.*, 118, 9901–9913, <https://doi.org/10.1002/jgrd.50778>, 2013.
- Rutan, D. A., Kato, S., Doelling, D. R., Rose, F. G., Nguyen, L. T., Caldwell, T. E., and Loeb, N. G.: CERES synoptic product: Methodology and validation of surface radiant flux, *J. Atmos. Ocean. Tech.*, 32, 1121–1143, <https://doi.org/10.1175/JTECH-D-14-00165.1>, 2015.
- Schuddeboom, A. J. and McDonald, A. J.: The Southern Ocean Radiative Bias, Cloud Compensating Errors, and Equilibrium Climate Sensitivity in CMIP6 Models, *Journal of Geophysical Research: Atmospheres*, 126, e2021JD035310, <https://doi.org/10.1029/2021JD035310>, 2021.
- Sengupta, M., Habte, A., Andreas, A., Reda, I., Jaker, S., Xie, Y., Yang, J., Gotseff, P., Kutchenreiter, M., and Shi, Y.: Sky Radiometers on Stand for Downwelling Radiation (SKYRAD60S), Atmospheric Radiation Measurement (ARM) User Facility [data set], <https://doi.org/10.5439/1377836>, 2016.
- Shakespeare, C. J. and Roderick, M. L.: The clear-sky downwelling long-wave radiation at the surface in current and future climates, *Q. J. Roy. Meteor. Soc.*, 147, 4251–4268, 2021.
- Shupe, M. D. and Intrieri, J. M.: Cloud radiative forcing of the Arctic surface: The influence of cloud properties, surface albedo, and solar zenith angle, *J. Climate*, 17, 616–628, [https://doi.org/10.1175/1520-0442\(2004\)017<0616:CRFOTA>2.0.CO;2](https://doi.org/10.1175/1520-0442(2004)017<0616:CRFOTA>2.0.CO;2), 2004.
- Stanford, M. W., Fridlind, A. M., Silber, I., Ackerman, A. S., Cesana, G., Mülmenstädt, J., Protat, A., Alexander, S., and McDonald, A.: Earth-system-model evaluation of cloud and precipitation occurrence for supercooled and warm clouds over the Southern Ocean's Macquarie Island, *Atmos. Chem. Phys.*, 23, 9037–9069, <https://doi.org/10.5194/acp-23-9037-2023>, 2023.
- Tan, I. and Storelvmo, T.: Sensitivity study on the influence of cloud microphysical parameters on mixed-phase cloud thermodynamic phase partitioning in CAM5, *J. Atmos. Sci.*, 73, 709–728, 2016.
- Tansey, E., Marchand, R., Protat, A., Alexander, S. P., and Ding, S.: Southern Ocean precipitation characteristics observed from CloudSat and ground instrumentation during the Macquarie Island Cloud & Radiation Experiment (MICRE): April 2016 to March 2017, *J. Geophys. Res.-Atmos.*, 127, e2021JD035370, <https://doi.org/10.1029/2021JD035370>, 2022.
- Trenberth, K. E. and Fasullo, J. T.: Simulation of present-day and twenty-first-century energy budgets of the southern oceans, *J. Climate*, 23, 440–454, <https://doi.org/10.1175/2009JCLI3152.1>, 2010.
- Trenberth, K. E., Fasullo, J. T., and Kiehl, J.: Earth's global energy budget, *B. Am. Meteorol. Soc.*, 90, 311–323, <https://doi.org/10.1175/2008BAMS2634.1>, 2009.
- Vergara-Temprado, J., Miltenberger, A. K., Furtado, K., Grosvenor, D. P., Shipway, B. J., Hill, A. A., Wilkinson, J. M., Field, P. R., Murray, B. J., and Carslaw, K. S.: Strong control of Southern Ocean cloud reflectivity by ice-nucleating particles, *P. Natl. Acad. Sci. USA*, 115, 2687–2692, 2018.
- Viúdez-Mora, A., Costa-Surós, M., Calbó, J., and González, J.: Modeling atmospheric longwave radiation at the surface during overcast skies: The role of cloud base height, *J. Geophys. Res.-Atmos.*, 120, 199–214, 2015.
- Wall, C. J., Hartmann, D. L., and Ma, P.-L.: Instantaneous linkages between clouds and large-scale meteorology over the Southern Ocean in observations and a climate model, *J. Climate*, 30, 9455–9474, 2017.
- Walters, D., Baran, A. J., Boutle, I., Brooks, M., Earnshaw, P., Edwards, J., Furtado, K., Hill, P., Lock, A., Manners, J., Morcrette, C., Mulcahy, J., Sanchez, C., Smith, C., Stratton, R., Tennant, W., Tomassini, L., Van Weverberg, K., Vosper, S., Willett, M., Browne, J., Bushell, A., Carslaw, K., Dalvi, M., Essery, R., Gedney, N., Hardiman, S., Johnson, B., Johnson, C., Jones, A., Jones, C., Mann, G., Milton, S., Rumbold, H., Sellar, A., Ujije, M., Whitall, M., Williams, K., and Zerroukat, M.: The Met Office Unified Model Global Atmosphere 7.0/7.1 and JULES Global Land 7.0 configurations, *Geosci. Model Dev.*, 12, 1909–1963, <https://doi.org/10.5194/gmd-12-1909-2019>, 2019.
- Wang, H., Klekociuk, A. R., French, W. J. R., Alexander, S. P., and Warner, T. A.: Measurements of cloud radiative effect across the Southern Ocean (43° S–79° S, 63° E–158° W), *Atmosphere*, 11, 949, <https://doi.org/10.3390/ATMOS11090949>, 2020.
- Wang, Z., Siems, S. T., Belusic, D., Manton, M. J., and Huang, Y.: A climatology of the precipitation over the Southern Ocean as observed at Macquarie Island, *J. Appl. Meteorol. Clim.*, 54, 2321–2337, <https://doi.org/10.1175/JAMC-D-14-0211.1>, 2015.
- Wild, M., Ohmura, A., Gilgen, H., Morcrette, J.-J., and Slingo, A.: Evaluation of downward longwave radiation in general circulation models, *J. Climate*, 14, 3227–3239, 2001.
- Wild, M., Long, C. N., and Ohmura, A.: Evaluation of clear-sky solar fluxes in GCMs participating in AMIP and IPCC-AR4 from a surface perspective, *J. Geophys. Res.-Atmos.*, 111, 1–15, <https://doi.org/10.1029/2005JD006118>, 2006.
- Williams, K. D. and Webb, M. J.: A quantitative performance assessment of cloud regimes in climate models, *Clim. Dynam.*, 33, 141–157, <https://doi.org/10.1007/s00382-008-0443-1>, 2009.
- Wilson, D. R., Bushell, A. C., Kerr-Munslow, A. M., Price, J. D., and Morcrette, C. J.: PC2: A prognostic cloud fraction and condensation scheme. I: Scheme description, *Q. J. Roy. Meteor. Soc.*, 134, 2093–2107, 2008.
- Yabuki, M., Shiobara, M., Nishinaka, K., and Kuji, M.: Development of a cloud detection method from whole-sky color images, *Polar Sci.*, 8, 315–326, 2014.
- Zelinka, M. D., Myers, T. A., McCoy, D. T., Po-Chedley, S., Caldwell, P. M., Ceppi, P., Klein, S. A., and Taylor, K. E.: Causes of higher climate sensitivity in CMIP6 models, *Geophys. Res. Lett.*, 47, e2019GL085782, <https://doi.org/10.1029/2019GL085782>, 2020.
- Zhang, X., Liang, S., Wang, G., Yao, Y., Jiang, B., and Cheng, J.: Evaluation of the reanalysis surface incident shortwave radiation products from NCEP, ECMWF, GSFC, and JMA using satellite and surface observations, *Remote Sens.-Basel*, 8, 225, <https://doi.org/10.3390/rs8030225>, 2016.